Journal of Sound and Vibration 434 (2018) 144–165

Contents lists available at ScienceDirect

Journal of Sound and Vibration

journal homepage: www.elsevier.com/locate/jsvi

Experimental study of the noise radiated by an air flow discharge through diaphragms and perforated plates

P. Laffay [a,b,*], S. Moreau [b,c], M.C. Jacob [b,d], J. Regnard [a]

[a] Safran Aircraft Engines, 77500, Moissy-Cramayel, France
[b] Université de Lyon, École Centrale de Lyon, F-69134, Écully, France
[c] Université de Sherbrooke, Sherbrooke, J1K2R1, Québec, Canada
[d] ISAE-SUPAERO, 31400, Toulouse, France

ARTICLE INFO

Article history:
Received 3 April 2018
Revised 19 June 2018
Accepted 23 July 2018
Available online 7 August 2018
Handling Editor: P. Joseph

Keywords:
Flow discharge
Diaphragms
Perforated plates
Jet noise
Jet interaction

ABSTRACT

An experimental analysis of the noise radiated by a high pressure flow discharge through diaphragms and perforated plates is carried out for a large range of subsonic and supersonic operating conditions (nozzle pressure ratio (NPR) from 1 to 3.6). A parametric study of the geometrical parameters is also achieved to characterize their influence onto the acoustic radiation and ways to reduce it. This reaches from single diaphragms to multi-perforated plates with variable hole diameters and arrangements that are placed at the exit of a duct. Different acoustic behaviors are observed: in all cases the far-field acoustic radiation is dominated by a broadband contribution associated with the turbulent mixing in shear layers. In the diaphragm cases, this broadband noise has similar characteristics as the mixing noise of classical unheated jets while in the multi-perforated plates cases, it is composed of two distinct humps associated with different parts of the jets development. For supersonic regimes, in addition to this broadband radiation, shock associated noise (screech and broadband shock associated noise) appears for all diaphragm cases and for the perforated plate with the closest holes. Finally for the smallest NPR, a high frequency tonal noise has been observed in most of the multi-perforated cases and for the smallest diaphragm. Different regimes of this radiation have also been observed with a possible amplitude modulation of the dominant tone. This radiation may be attributed to vortex shedding due to the sharp section reduction that would trigger a flow resonance between the small ducts of the holes and their sharp edges.

1. Introduction

In a large number of industrial sectors, it is possible to find pressure-release systems aiming to reduce the pressure or simply to discharge a flow under pressure: steam valves in power plants, industrial pneumatic air systems, sterilization of medical devices… In many cases, the pressure drop is generated by placing diaphragms or perforated plates in the flow. The addition of such devices creates a strong differential pressure between both sides of the element and generates high speed jets. These jets are responsible for a significant acoustic radiation. The aim of the present study is to analyze the different acoustic radiation mechanisms that may appear during the discharge of a high-pressure flow through diaphragms and perforated plates.

Jet noise being an importante sources of noise in many systems such as aircraft, it has been extensively studied since 1950's analytically, experimentally and numerically for both subsonic and supersonic regimes (mean jet velocity U_j smaller and greater

* Corresponding author. Safran Aircraft Engines, 77500, Moissy-Cramayel, France.
E-mail address: paul.laffay@safrangroup.com (P. Laffay).

https://doi.org/10.1016/j.jsv.2018.07.036
0022-460X/

than the speed of sound respectively). An important criterion in jet noise is the Reynolds number based on the jet diameter D: $Re_D = U_j D/\nu$ where ν is the kinematic viscosity of the fluid. It allows defining the state of the initial boundary layer at the nozzle exit. Indeed below about 2.5×10^5, the jet is most likely laminar which yields vortex pairings responsible for a higher sound radiation [1]. In the present study the Reynolds number is always greater than 2.5×10^5. For these jets the acoustic radiation is dominated by a broadband component called mixing noise. It is composed of two distinct contributions associated with large coherent turbulent structures and small scale turbulence which develop in the shear layer. In the case of subsonic jets the first source is produced by the periodic intrusion of large coherent structures at the end of the jet potential core [2,3] while for supersonic jets, it is mainly due to Mach wave radiation induced by the supersonic convection of these structures [4,5]. This source mainly radiates in the downstream direction and the maximum amplitude is obtained for a Strouhal number $St = fD/U_j \simeq 0.2$ for unheated jets where f is the frequency [3,6,7]. It physically represents the passing frequency of the large coherent structures. The source associated with the small scale turbulence however is omnidirectionnal and is maximum for $St \simeq 0.3$ [3]. For supersonic jets, when the outlet pressure is different from the ambient pressure, shock cells are formed in order to adapt the two pressures and are responsible for the appearance of a new source called shock-associated noise. It is composed of a tonal contribution, the screech and a broadband one, the broadband shock associated noise (BBSAN). Due to its high acoustic level, the first one has been extensively studied since 1950's although no consensus has yet been reached [8–12]. Despite this, the various works agree that the screech is generated by a feedback loop process: turbulent instabilities are created on the nozzle lips and develop and grow in the shear layer. The interaction of these instabilities with the shock cells generates a sound wave which propagates back the nozzle lips and disrupts the initial shear layer creating new instabilities thus closing the loop. The BBSAN is also caused by the interaction of these instabilities with the shock cells but without feedback loop [13–15].

Perforated plates or more generally multi-hole nozzles, although acoustically very interesting with respect to a single jet of similar cross-section have been hardly investigated. Among the few existing studies, Atvars et al. [16,18] measured the acoustics benefits of multitube nozzle and acoustically lined ejectors compared to a single one for supersonic regimes. They observed a reduction up to 16 PNdB for less than 1% loss of thrust for these nozzle geometries. They have modeled the broadband component of the multitube nozzle noise as the contribution of two distinct sources. The first one called "pre-merging (and merging) turbulence noise" is responsible for the high frequency part of the spectra and is produced, as indicated by its name, by the turbulence of the isolated small jets and merging region (where the small jets interact with each other). The second source is produced by turbulence of the post-merged region (called "post-merged turbulence noise") and is responsible for the low frequency part of the acoustic spectra (Fig. 1(a)). In 1978, Regan and Meecham [19,20] tried to understand the origin of the noise reduction induced by a multitube nozzle compared with a single one with equal thrust for Mach numbers up to 0.99. Their work is based on the study of correlation between jet pressure fluctuations and far field acoustic measurements. Static pressure fluctuations are measured with a calibrated high-temperature acoustically damped probe tube. They observed a reduction of the turbulence intensity in excess of 20% for the tested multitube nozzles compared with a conventional single one with similar thrust. They therefore explained the acoustic reduction by this diminution of the turbulence intensity in the jet. Correlation measurements have also shown that the high-frequency far-field acoustic radiation is mainly generated by the outer jets. The sound radiated by the inner jets is strongly refracted by high velocity neighboring jets. Similar conclusion has been observed by Gray et al. [21] for high velocity jets (sonic and above). For low velocities however they observed a lower shielding induced by external jets. For these cases, the total sound power approaches the sum of all isolated jet contributions. They have thus attempted to define by a geometric scaling analysis the number of equivalent jets that allows to predict the acoustic level of the pre-merging region (this criterion gives an information on the shielding level of the external jets). Other authors have also attempted to define an empirical relation of the "effective" number of jet [22–24]. More recently Sheen and Hsiao [17,25] studied the effect on the noise level of the exit spacing in a multiple-jet nozzle at high velocities for application to industrial pneumatic air systems. They observed that increasing the exit spacing shifts the sound spectrum to the low frequencies while reducing it shifts it to the high frequencies. This shift toward high frequencies allows reducing the noise in the audible range. They conclude that due to these two opposite effects, for a multiple-jet nozzle with a limited size, there is an optimized geometry that generates the lowest sound pressure level in the audible range. Based on their measurements, they proposed a model of the multiple-jet nozzle noise shown in Fig. 1(b). The low frequency part of the multiple-jet nozzle spectrum is similar to that of a single jet with similar thrust while the high frequency part is obtained by shifting the single-jet spectrum toward the high frequency side. In between there is a transitional region that remains poorly known. Sheen and Hsiao also noted that the thrust reduction of a multi-jet nozzle compared with a single one with similar cross section is very low.

The present study is divided into five parts. In the first one, a description of the experimental setup is given. In the second section, the various acoustic measurements are presented in order to identify the different acoustic behaviors which appear during the discharge of a high-pressure flow through diaphragms and perforated plates. Finally, The last three parts study are devoted to a detailed analysis of these different phenomena.

2. Experimental setup

Measurements have been carried out in the supersonic open jet wind tunnel of the École Centrale de Lyon. The experimental device is composed of a Centac C60MX2-SH centrifugal compressor from Ingersoll Rand allowing to compress air at 4.2 bars with a nominal mass-flow rate of 1 kg s^{-1}. The pressurized air is then directed to a Donaldson DV 5500 WP dryer which reduces the dew point. The flow then passes through a butterfly valve allowing to control the operating regime of the wind tunnel. The flow finally opens into an $10 \times 8 \times 8$ m large anechoic room in which is placed the simplified test valve. The latter is

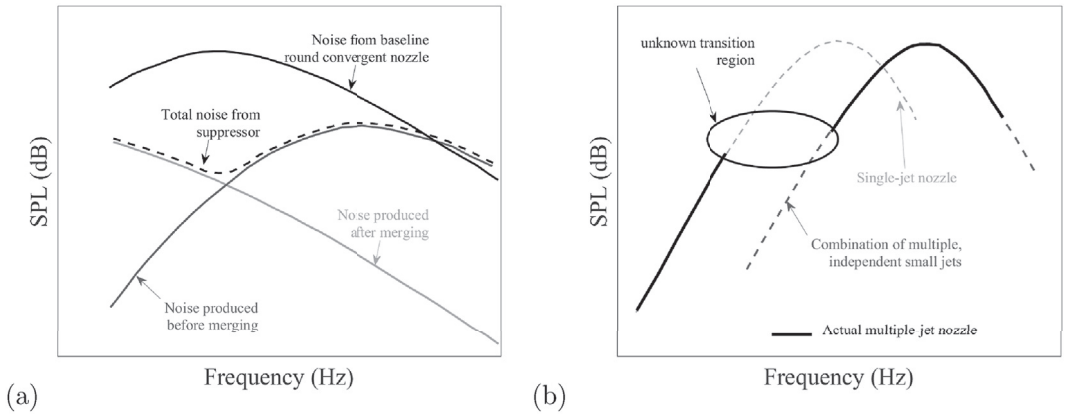

Fig. 1. (a) Multitube noise model from Atvars et al. [16] and (b) model of the multiple-jet nozzle noise according to Sheen [17].

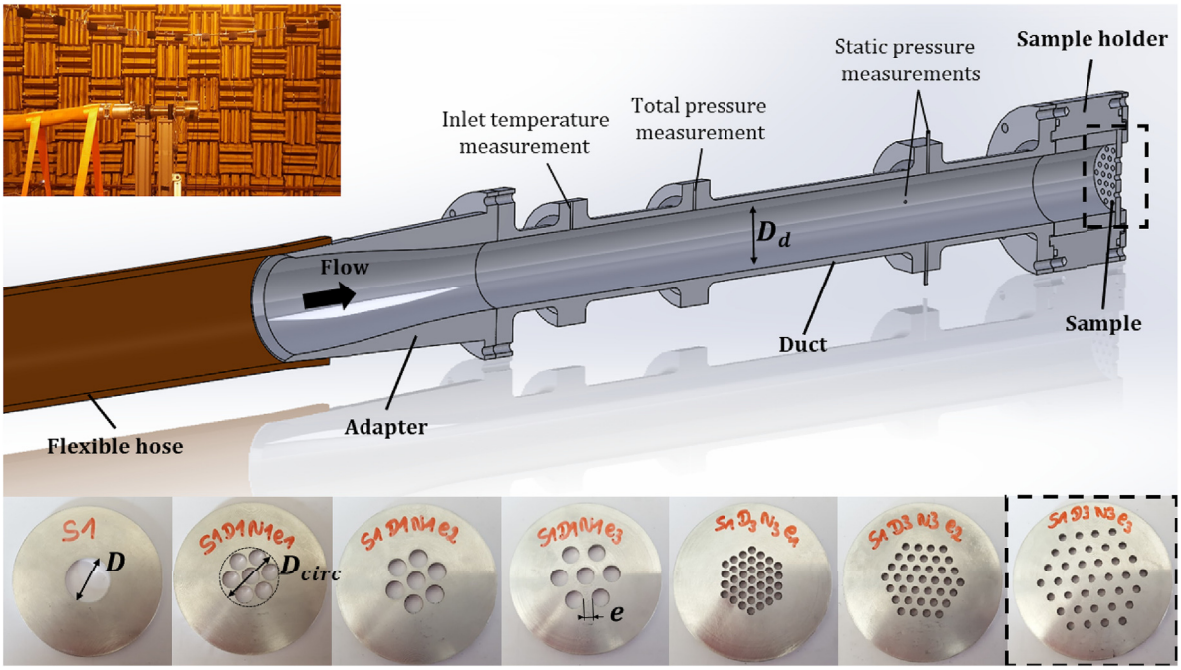

Fig. 2. Experimental setup.

composed of a D_d internal diameter and $6D_d$ long inlet duct (cross-section S_d) opening on a sample holder allowing to insert different diaphragms or perforated plates which will generate more or less severe pressure drops (Fig. 2). The pressurized air is conveyed to the valve by means of a $1.6D_d$ diameter flexible hose and an adaptation part allowing to gradually adjust the flow to the duct diameter. A total pressure and four static pressure taps (distributed over the circumference) are arranged on the inlet duct in order to determine the operating condition of the valve. It is defined by the ratio of the total pressure p_t at the inlet of the valve to the ambient pressure in the anechoic room p_a and is called Nozzle Pressure Ratio (NPR). The static and total pressure measurements are carried out with Valydine DP-15 differential sensors associated with Nr. 46 membrane allowing pressure up to 350000 Pa. Total temperature T_t measurements are also made at the inlet and outlet of the valve using K-type thermocouples.

17 samples (3 diaphragms and 14 perforated plates) have been tested. Part of the tested samples is shown in Fig. 2 and their geometrical characteristics are defined in Table 1. All the geometric parameters are normalized by the dimensions of the upstream duct. Each sample is characterized by the total surface of the perforations S, the number of perforations N, the diameter of these perforations D and their mutual spacing e. The last parameter D_{circ} given in Table 1 corresponds to the smallest diameter encircling the perforations of the plates (circumscribed circle). The geometry of these different perforated plates and diaphragms has been defined by trying to vary only one parameter at a time (of course, for a constant cross-section S, the parameters N and D are linked). The grids S1D2N2e3div/fillet are similar to S1D2N2e3 but with a modified perforation geometry. Indeed the former

Table 1
Geometric description of the tested diaphragms and perforated plates.

Name	N	$D/D_d \times 10^{-1}$	$e/D_d \times 10^{-1}$	$S/S_d \times 10^{-1}$	$D_{circ}/D_d \times 10^{-1}$
S1	1	4.31	–	1.86	–
S1D1N1e1	7	1.63	0.20	1.86	5.29
S1D1N1e2	7	1.63	0.41	1.86	5.70
S1D1N1e3	7	1.63	0.82	1.86	6.52
S1D2N2e1	19	0.99	0.20	1.86	5.75
S1D2N2e2	19	0.99	0.41	1.86	6.57
S1D2N2e3/div/fillet	19	0.99	0.82	1.86	8.20
S1D3N3e1	37	0.71	0.20	1.86	6.18
S1D3N3e2	37	0.71	0.41	1.86	7.41
S1D3N3e3	37	0.71	0.82	1.86	9.86
S2	1	2.61	–	0.68	–
S2D2N1e1	7	0.99	0.20	0.68	3.37
S3	1	6.01	–	3.61	–
S3D2N3e1	37	0.99	0.20	3.61	8.14
S4D4N4e4	351	0.31	0.06	3.29	1.00

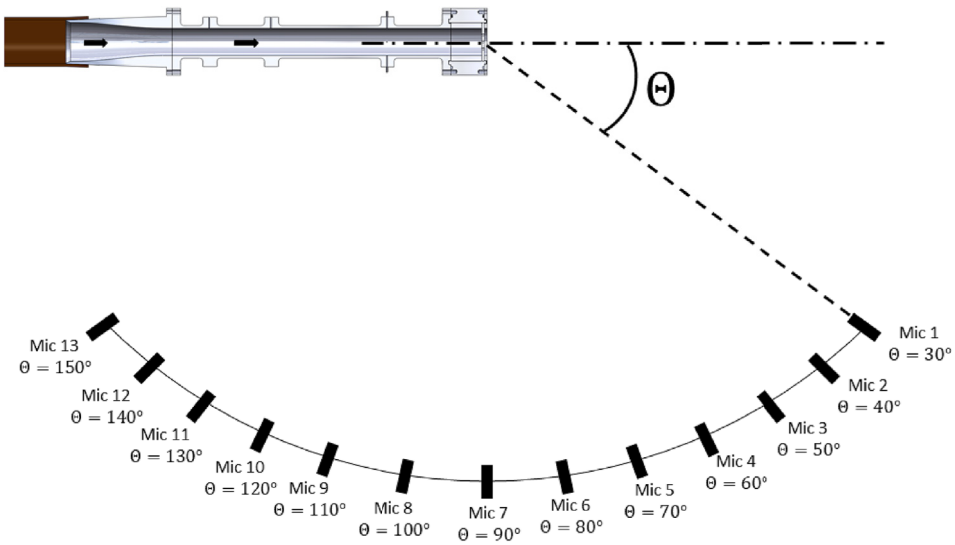

Fig. 3. Definition of the observation angle Θ.

have a divergent form (going from a $0.099D_d$ diameter at the entrance to a $0.140D_d$ diameter at the exit) while a $0.041D_d$ radius fillet is added on the exit edge of the second. The grid S4D4N4e4 has been studied to make comparisons with previous measurements. Finally all the perforated plates and diaphragms have a thickness of $0.092D_d$.

Measurements were made for NPRs ranging from 1 to 3.6 by steps of 0.2. NPR $=$ 1 corresponds to a case without flow and provides the background noise of the installation (wind tunnel on but closed butterfly valve). The flow is unheated which means that the reservoir temperature T_r is equal to the ambient pressure T_a. The far-field acoustic measurements are carried out using a 2 m radius circular array centered on the outlet of the valve. For a frequency analysis between 100 Hz and 40000 Hz, this distance corresponds to 0.59λ and 235λ respectively, λ being the acoustical wavelength. The far-field is reached for $R \gtrsim \lambda$ i.e. $f \gtrsim 170$ Hz where k is the wave number and R the antenna radius. This array is composed of 131/4 inch PCB microphones allowing to cover angles ranging from $\Theta = 30°$ to 150° by steps of 10° with Θ defined with respect to the valve axis starting from the downstream position (Fig. 3). The microphones have a normal incidence and their protective grid caps have been removed in order not to disturb the high frequency acoustic measurements [26]. Acoustic signals are acquired during 30 s at a 102400 Hz sampling rate and the static pressure measurements are obtained by averaging a 5 s signal sampled at 5000 Hz. These acquisition times are sufficient to ensure the statistical convergence of the subsequent data analysis. These signals are recorded with a National Instrument PXI-1006 acquisition system equipped with NI-PXI 4472 cards. The total pressure and temperature at inlet and outlet are continuously recorded using a National Instrument cDAQ 9174 acquisition system to have a real time information of the wind-tunnel operating point.

3. Experimental results

3.1. Far-field acoustic radiation

Far-field acoustic measurements are first presented for different samples and NPR tested in order to identify the different acoustic behaviors. Power spectral density (PSD) of the acoustic signals (S_{pp}) is obtained with the cpsd matlab function which allows to calculate an autospectrum of the temporal acoustic signal by Welch's periodogram method. The segments have $F_s/8$ elements for a frequency resolution of $\Delta f = 8$ Hz. A Hanning window and 50% overlap are used. The sound pressure level (SPL) is calculated by the following relation:

$$SPL(f) = 10\log\left(\frac{S_{pp}\Delta f}{p_{ref}^2}\right)[\text{dB}], \tag{1}$$

where $p_{ref} = 2 \times 10^{-5}$ Pa is the reference acoustic pressure. The directivity curves are obtained by calculating the OASPL value of each microphone signal between $f_{min} = 100$ Hz and $f_{max} = 40000$ Hz. This value is obtained by the following relation:

$$OASPL = 10\log\left(\frac{\sum_{f_{min}}^{f_{max}} S_{pp}(f)\Delta f}{p_{ref}^2}\right)[\text{dB}], \tag{2}$$

3.1.1. Diaphragms

Diaphragms are commonly used devices in industry to measure a mass-flow rate or, as in the present case, to relax/discharge a fluid under pressure. In most cases, diaphragms are placed inside a duct which modifies the sound generation and radiation. However, when the latter is placed at the end of the duct, it may be responsible for a very important acoustic radiation into the surrounding medium at rest. Although the cross-sectional reduction within a diaphragm is abrupt, the outlet geometry remains close to that of a conventional nozzle. Similar acoustic features are thus expected. Fig. 4 shows the far-field acoustic spectra as a function of the observation angle Θ and NPR for the 3 tested diaphragms. First, for low NPRs, the acoustic radiation in Fig. 4(a), (c) and (e) is dominated by a broadband noise component for the three diaphragms (see Sec. 4). For S2, high frequency tones appear in addition to a middle frequency hump and tone at NPR = 1.2. The high frequencies tones remain at NPR = 1.4 (not plotted here) and NPR = 1.6. This tonal noise is studied in Sec. 6. For higher NPR (NPR > 2.2), the broadband noise is associated with a high frequency hump and several high intensity tones. The directivity of these two acoustic features is given in the radiation maps 4(b), (d) and (f). The frequency of the tonal noise does not vary as a function of the observation angle while the high frequency hump decreases in frequency when Θ is increased. The directivity of these two sources suggests a screech and BBSAN respectively which is characteristic of an underexpanded supersonic jet [8,12,13]. This acoustic radiation is studied in Sec. 5. The background noise given by the black curve (NPR 1) remains very low compared with the measurements even at low NPR.

3.1.2. Perforated plates

As discussed in the introduction, perforated plates or more generally multihole nozzles have been mainly studied in order to reduce the jet noise on aircraft engines. Indeed the reduction of the perforation size and the increase of their number allow not only to reduce the acoustic radiation due to the shielding effects but also to shift it towards high frequencies, which has the effect of reducing the radiation in the audible range and increasing atmospheric attenuation [16–20]. Similar observations are therefore expected in the case of perforated plates with respect to a diaphragm of equivalent cross-section. Fig. 5 that shows the far-field sound spectra at Θ = 90° and at different NPR for four perforated plates confirms this acoustic behavior. As for diaphragms: far-field acoustic spectra are dominated by a broadband component but with higher levels at high frequencies. On top of this, the high frequency tonal noise observed for diaphragm S2 appears for all perforated plates but its amplitude varies strongly depending on the considered plate. Moreover, with a divergent shape (Fig. 5(b)) or a filleted outlet of the perforations (not shown here) this phenomenon persists for higher NPRs (up to NPR 1.2 for S1D2N2e3 in Fig. 5(a) and NPR 1.8 for S1D2N2e3div in Fig. 5(b)). For high NPR, the shock associated noise is strongly reduced and even suppressed in most of the cases. In fact, for all tested grids, screech radiation has been observed for the plate S4D4N4e4 only (Fig. 5(d)), which is composed of 351 very close holes.

The effect of the perforation parameters (perforation size, spacing, number) on the sound radiation is now studied. Fig. 6 (a), (c) and (e) give far-field spectra of grids with similar cross section S, perforation number N and perforation size D but with various perforation spacings e for NPR = 1.6. Fig. 6 (b), (d) and (f) however compare the noise radiated from grids with similar e and S but various N and D. A comparison with the equivalent diaphragm is also given in each case. Spectra are given for an observation angle $\theta = 30°$ so that the mixing noise hump is more pronounced [27]. Firstly, the perforated plates allow reducing the broadband radiation at low and medium frequencies very significantly compared with the equivalent diaphragm. As observed in Refs. [16–20], the levels at high frequencies are however increased by the reduction of the perforation sizes. The low NPR tonal noise also seems to appear more regularly and up to higher NPR when perforated plates are mounted and preferably for larger perforation diameter (Fig. 6 (a)). Moreover, the double hump discussed in the introduction [16–18,25] is

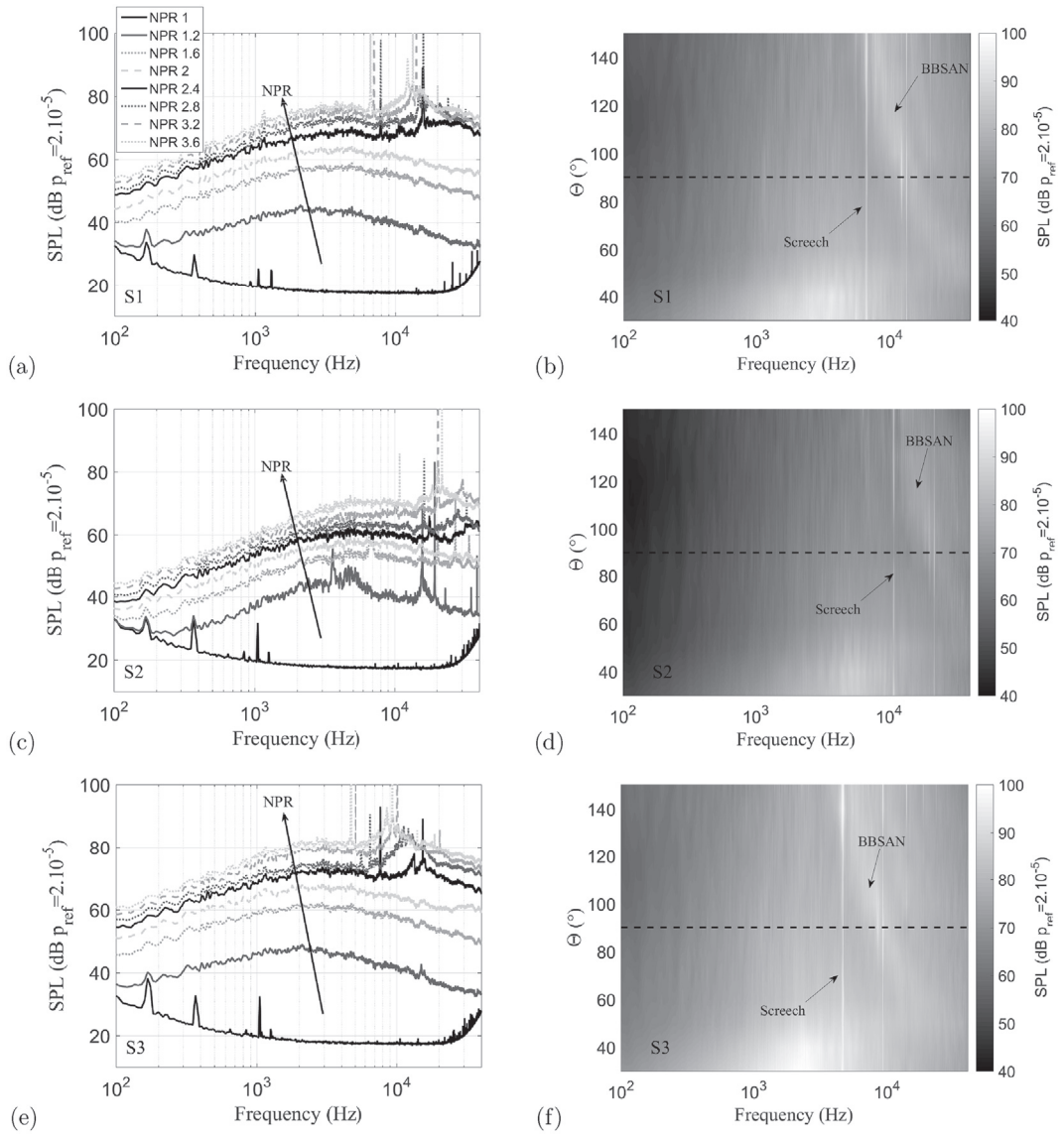

Fig. 4. Far-field acoustic spectra as a function of the NPR at $\Theta = 90°$ for diaphragms: (a) S1, (c) S2 and (e) S3. Maps of the far-field acoustic spectra as a function of Θ at NPR = 3.6 for: (b) S1,(d) S2 and (f) S3.

clearly visible. The first hump at medium frequencies will hereafter be referred to as the post-merging hump (PMH) and the second at higher frequencies the merging hump (MH).

By varying e for a constant S, D and N (Fig. 6 (a), (c) and (e)), an amplitude decrease of PMH and at the same time an increase of MH can be observed. Moreover, from a spectral view, the PMH is shifted to the low frequencies when the perforation spacing is increased while the MH does not seem to be strongly affected. This observation agrees with the results of Sheen [17,25]. The increase of the perforation spacing seems to transfer some of the acoustic energy from PMH to MH. This can be explained by the fact that increasing e delays the merging of the jets, a greater part of the turbulence develops like that of an isolated jet which is responsible for MH. MH is then increased while PMH is decreased. Moreover, the increase of the perforation spacing also generates an increase of the post-merging jet diameter which induces a shift to the lower frequency of its mixing noise characterized by $St = fD/U_j = 0.2$ at $\Theta = 30°$ and finally a shift of the PMH frequency. It is probably also associated with a slight reduction of the mean velocity in the final mixed jet.

By now decreasing D and increasing N for constant S and e, PMH is again reduced and shifted toward the low frequencies. Indeed, similarly as for the increase of e, decreasing D and increasing N at a constant cross section and a constant spacing induces an increase of the post merging jet diameter. A good indicator of this increase is given by the size of the circumscribed circle D_{circ} given in Table 1. Moreover, the reduction of D shortens the potential core resulting in a more rapid velocity decay. The turbulent intensity in the post-merging jet is thus decreased due to the faster turbulence scale reduction, the slower eddy convection and

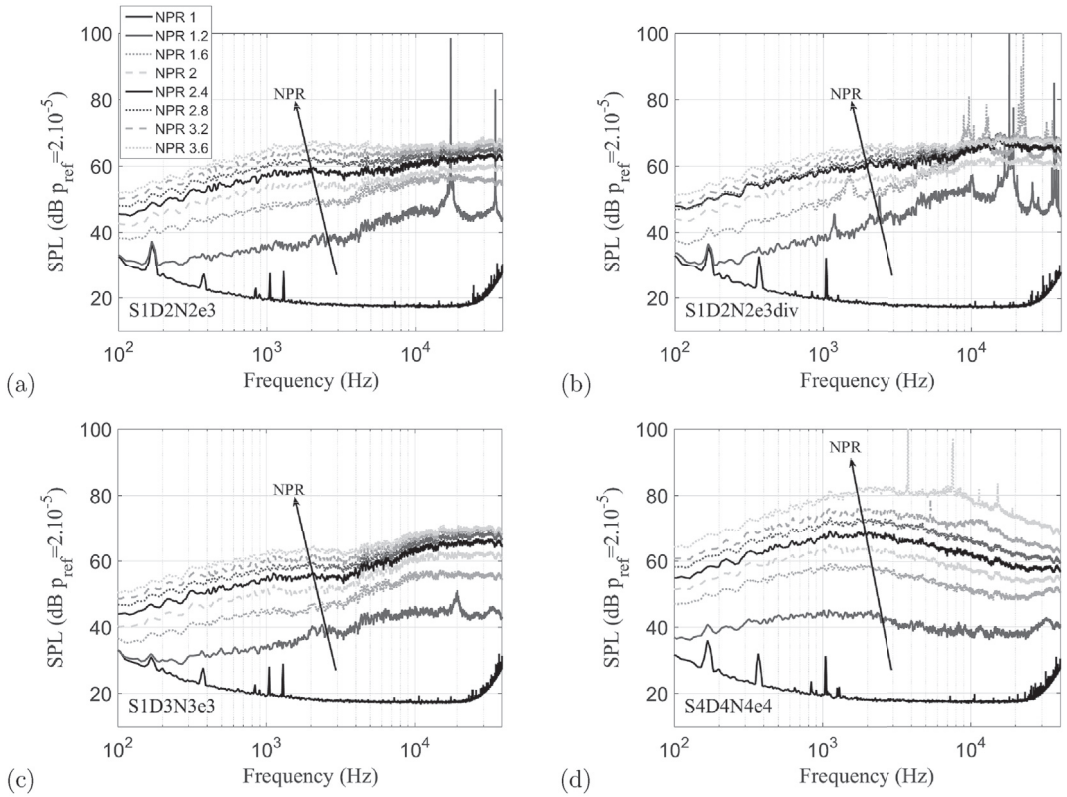

Fig. 5. Far-field acoustic spectra as a function of the NPR at $\Theta = 90°$ for (a) S1D2N2e3, (b) S1D2N2e3div, (c) S1D3N3e3 and (d) S4D4N4e4.

a more efficient mixing which finally reduces the PMH level. Similarly, these modifications of D and N have also the effect of slightly decreasing the MH level in most of the cases. In fact, two opposite phenomena most likely come into play here. The increase of N induces an increase of the number of outer jets responsible for MH which should therefore increase. However, the reduction of the small jet sizes also leads to a reduction of the acoustic radiation of these jets caused by the reduction of their global turbulent energy which should therefore decrease MH [28]. The reduction of D is likely to explain also a shift of MH towards the high frequencies although it is not always clearly visible in the presented spectra because of the logarithmic scale.

The radiation of perforated plates can now be adapted by varying these various parameters: an increase of e (with a constant D and N) allows to increase the MH levels and decrease the PMH one while shifting the latter towards low frequencies. The reduction of D (with constant e and N) shifts MH towards high frequencies and reduces the two humps. Finally an increase of N (with constant e and D) should increase the two humps and shift PMH to low frequencies. Therefore, for some applications the optimum combination can be a balance between the two hump levels in order to reduce the maximum mixing noise of the perforated plate considered as for S1D3N3e2 (Fig. 6(d) and (e)). For other applications however, a transfer of the maximum of the acoustic radiation to the high frequency hump can be more interesting to reduce the acoustic energy in the audible range and to attenuate the noise radiation more quickly thanks to atmospheric viscous dissipation or liner absorption.

The modification of the grid parameters thus allows to strongly modify the acoustic spectrum at 30°. To see the effect at other radiation angles, Fig. 7 gives the OASPL directivity between 100 Hz and 40000 Hz for plates with various parameters at NPR = 1.6. These directivity plots show a significant modification of the sound directivity of the perforated plates compared with the equivalent diaphragm (dash black curve), in particular for plates with spaced perforations. Indeed, for diaphragms, the sound radiation dominates downstream. This result is typical of a jet mixing noise for which the radiation of the large downstream turbulent structures dominates [2,4]. For perforated plates with close perforations (Fig. 7(b)), a rather similar directivity can be observed despite a slight reduction of the radiation upstream and downstream. Remember that for these plates, the acoustic radiation is dominated by the PMH associated with the radiation of post-merged region. Therefore the radiation of this region seems to retain the directivity characteristics of the jet mixing noise.

By now increasing e for a constant N, D and S a significant increase of the sound radiation appears between $\Theta = 40°$ and 110° compared to the previous cases (Fig. 7(a) and (c)). Two distinct lobes also seem to emerge at 50° and 70°. This suggests a modification of the sources responsible for this radiation. The increase of the sideline sound is very clear on plates with the

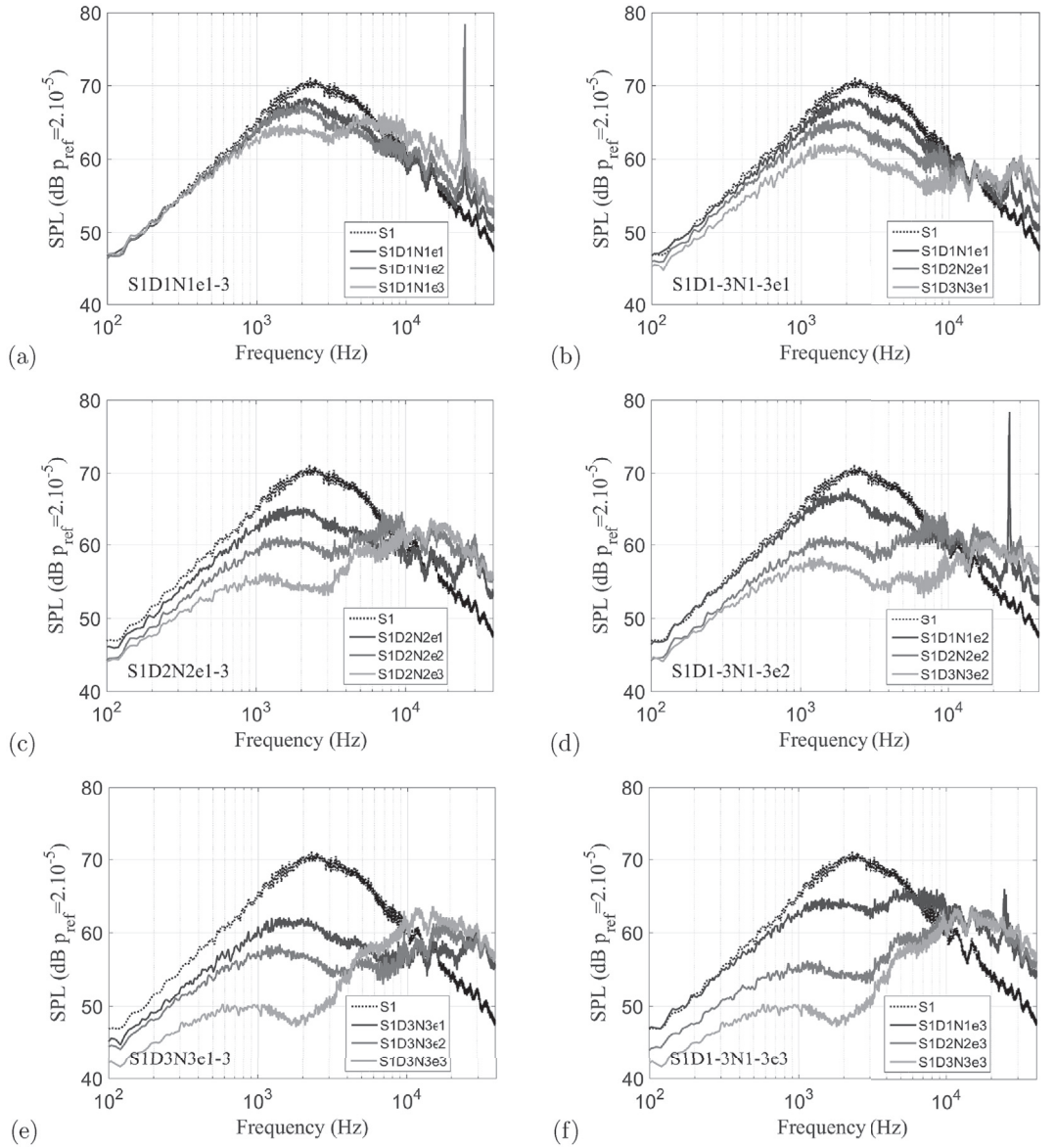

Fig. 6. Far-field acoustic spectra as a function of perforated plate geometric parameters at $\Theta = 30°$ and NPR = 1.6 for: (a),(c),(e) perforated plates with different perforation spacing S1D1N1e1-3, S1D2N2e1-3 and S1D3N3e1-3 respectively; (b),(d),(f) perforated plates with different perforation diameter and number S1D1-3N1-3e1, S1D1-3N1-3e2 and S1D1-3N1-3e3 respectively.

largest perforation spacing shown in Fig. 7(d). It also seems that the reduction of the perforation diameters accentuates this phenomenon. As a reminder, the increase of e and the reduction of D allow to increase the emergence of MH associated with the radiation of the pre-merging and merging zones. Therefore the acoustic sources associated with the radiation of these two zones seem to be slightly modified compared with a classical jet mixing noise. An additional analysis of this acoustic radiation is carried out in Sec. 4.

Despite the increase of the acoustic power between 100 and 40000 Hz for the latter plate cases, it is important to mention that for these same configurations a significant reduction of the OASPL has been observed in the audible range (between 100 and 20000 Hz). Indeed, as shown in Fig. 6, the increase of e and the reduction of D allow to increase MH and decrease PMH due to the late merging of the isolated jets. Part of MH being outside of the audible range, the acoustic power of the latter is then reduced. This result is consistent with the work of Sheen and Hsiao [17,25]. Moreover, MH being in this case only partially taken into account, the increase of the acoustic radiation in the sideline direction is not significant.

The different acoustic behaviors observed in the present study as a function of the geometry and operating point are then summarized in Fig. 8. Each of these acoustic phenomena will be studied in more detail in the following sections.

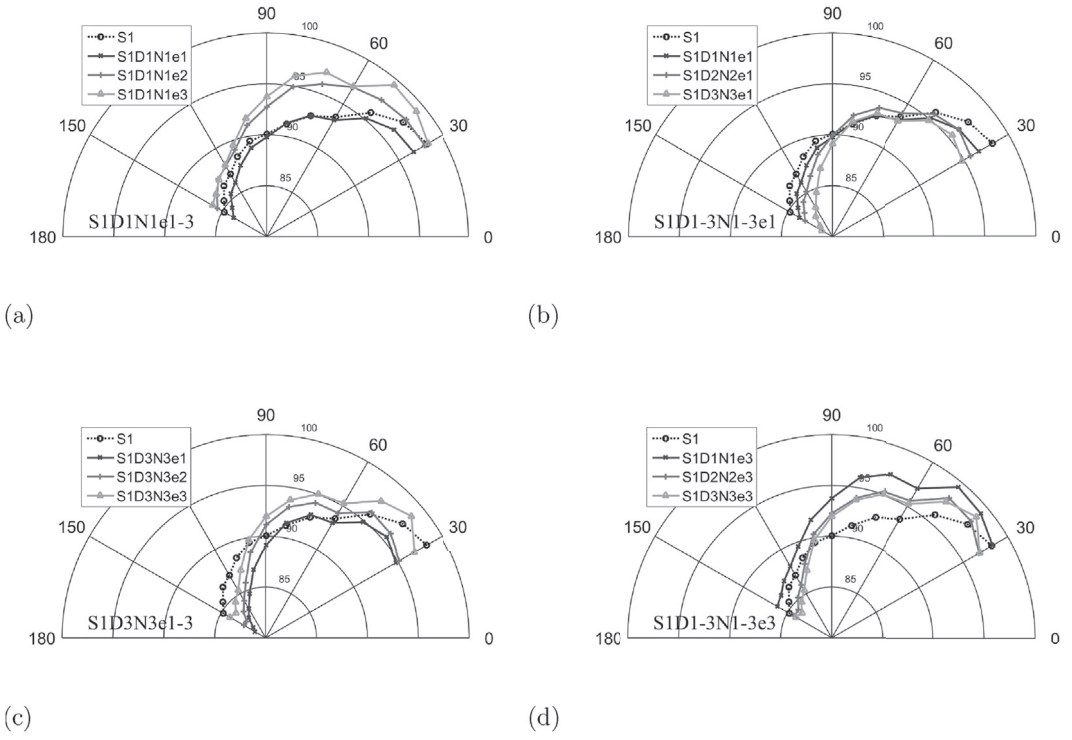

Fig. 7. OASPL directivity as a function of Θ at NPR = 1.6 for: (a),(c) perforated plates with different perforation spacing S1D1N1e1-3 and S1D3N3e1-3 respectively; (b),(d) perforated plates with different perforation diameter and number S1D1-3N1-3e1 and S1D1-3N1-3e3 respectively.

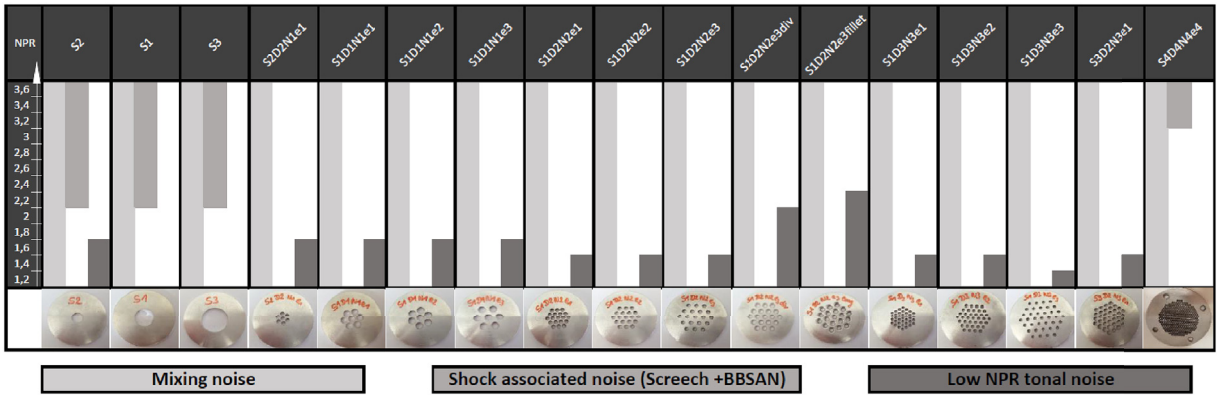

Fig. 8. Summary of the different acoustic behaviors observed on the present study.

3.2. Mass-flow rate measurements

The previous acoustic comparisons have been carried out for a constant NPR and cross-section S. However, the noise reduction generated by the perforated plates might be related to the geometry alone or also to a performance reduction. In the case of fluid discharge, one of the main performance criterion is the mass-flow rate q_m. Indeed, the increase of the perforation number for a constant cross-section might naturally generate a reduction of the mass-flow rate due to the *vena contracta* effects. However, the flow being strongly compressed upstream of the grids, this phenomenon might be negligible. In order to evaluate this possible mass-flow reduction, the mass flow rate is calculated by considering the total pressure p_t, the static pressure p_s and the total temperature T_t at the inlet of the valve. The flow is assumed to be isentropic and uniform over the entire valve cross-section (1D), which implies that the boundary layers are neglected. With these assumptions, the mean static pressure is uniform though the duct cross-section. The mean static pressures recorded over the circumference of the valve and shown in Fig. 9 (a) are identical, which is consistent with these assumptions. The Mach number M_j of the flow upstream of the grid can

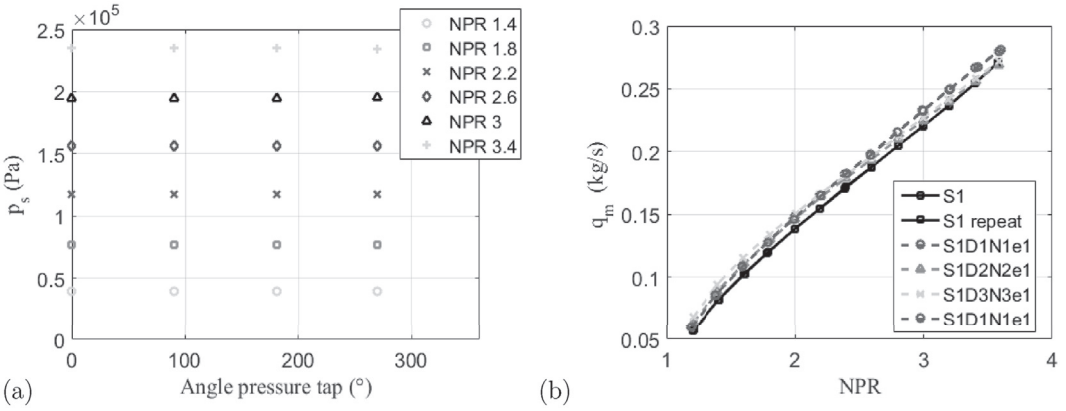

Fig. 9. (a) Evolution of the static pressure over the circumference of the inlet duct of the valve and (b) evolution of the mass-flow rate for different perforated plates and diaphragms with similar *S* but different *N*.

then be calculated considering the following isentropical relationship:

$$M_j = \sqrt{\frac{2}{\gamma - 1}\left(\mathrm{NPR}^{\frac{\gamma-1}{\gamma}} - 1\right)}, \tag{3}$$

γ being the heat capacity ratio. From M_j and T_t at the inlet of the valve, the static temperature T_j can now be obtained with:

$$T_j = \frac{T_t}{1 + M_j^2 (\gamma - 1)/2}. \tag{4}$$

The flow velocity U_j is then:

$$U_j = M_j \sqrt{\gamma r T_j}, \tag{5}$$

with r the specific gas constant. Finally, neglecting the boundary layers, the mass-flow rate q_m can be calculated by:

$$q_m = \rho_j U_j S_{inlet}, \tag{6}$$

where $\rho_j = \frac{P_s}{rT_j}$ is the density of the flow at the inlet section of the valve and S_{inlet} the surface of this section. The mass-flow rate for different perforated plates and diaphragms with similar cross-section but different perforation number is thus plotted in Fig. 9 (b). In the same figure, a repeatability test is also plotted in the case of the diaphragm (S1 repeat). This measurement has been made at a different day and superimposes perfectly with the latter which testifies to a very good repeatability of these mass-flow rate measurements. A good conservation of the mass-flow rate between the different perforated plates and diaphragms of equivalent cross-section can be observed. The increase of the perforation number does not seem to reduce the mass-flow rate due to the *vena contracta* effects. The slight variations that can be observed mainly at high NPR are probably caused by small modifications of the flow in the different cases.

4. Mixing noise study

In the case of diaphragms and perforated plates, similar acoustic behaviors as found in more conventional nozzles have been observed. Therefore mixing noise, which constitutes the main broadband part of jet noise, is first considered for the present valve.

4.1. Diaphragms

As explained in the introduction jet mixing noise is associated with the radiation of two distinct sources: the first one, associated with the large coherent structures which mainly radiate in the downstream direction and the second one, attributed to the radiation of the small scale turbulence in the shear layer which is omnidirectionnal [2–5]. In order to identify these two sources, the same procedure as that used by Tam et al. [4] for the subsonic and perfectly expanded supersonic jets is followed: the autocorrelation and intercorrelation of the acoustic signals measured in the far-field is carried out.

The autocorrelation function first allows to give information on the correlation level between a given signal and the same signal delayed in time revealing the causal linear link between the two signals: it thus measures the duration of an organized event contained in the signal. In the case of an acoustic signal, this post-processing will then inform about the spatial correlation

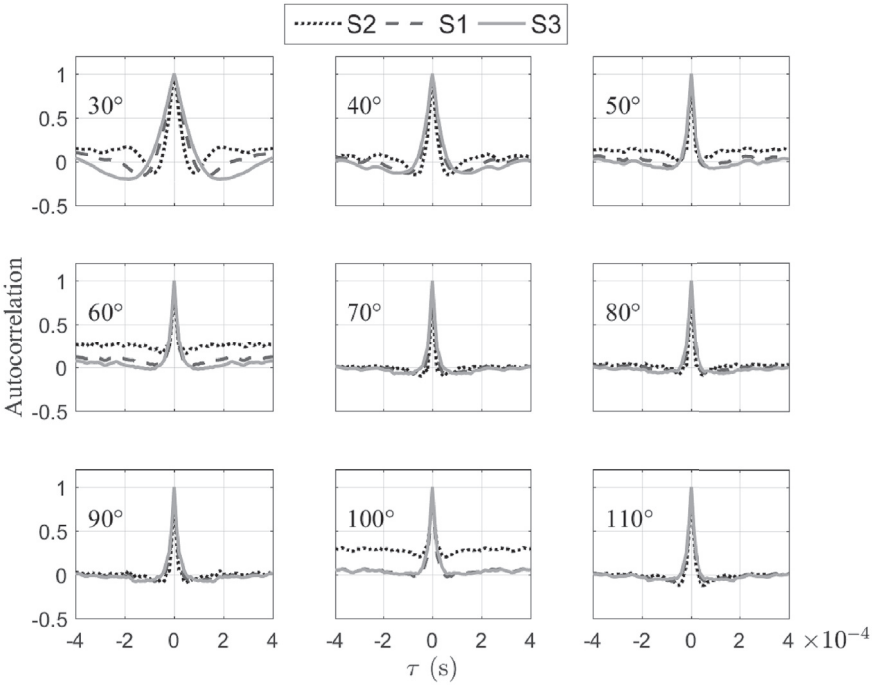

Fig. 10. Normalized autocorrelation at NPR = 1.8 for the three tested diaphragms.

of the acoustic radiation in its propagation direction. In the present case, this direction corresponds to the radial direction. The autocorrelation R_{nn} is expressed by:

$$R_{nn}(\tau) = \frac{\langle p_n(t)p_n(t+\tau)\rangle}{\langle p_n^2(t)\rangle}, \tag{7}$$

where $p(t)$ is the pressure time signal, τ the temporal delay, n the microphone considered and $\langle\rangle$ denotes the time average. Fig. 10 gives the normalized autocorrelation on the first nine microphones (30°–110°) for the three tested diaphragms at NPR = 1.8.

As observed by Tam et al. [4], a very different behavior appears between the first two microphones placed in the downstream direction and the others. The autocorrelation peak on these first microphones is much wider than on the following and is framed by a negative zone reflecting an increase of the correlation over time and therefore over the wave propagation direction. This result is consistent with the hypothesis of the dual source responsible for jet mixing noise. Indeed, the large turbulent structures can be naturally assumed to generate spatially larger acoustic disturbances which are therefore correlated over a longer period of time in particular in their preferred propagation direction. Small-scale turbulence, on the other hand, produces much smaller and therefore less coherent perturbations. The negative part framing the autocorrelation peak can be easily understood by considering an acoustic perturbation as the succession of a compression wave (positive pressure) and an expansion wave (negative pressure). For the microphone n, the product $p_n(t)p_n(t+\tau)$ then becomes negative when the delay τ reflects two opposite phases. The negative part thus stands for a coherence zone with two opposite phases. This phenomenon is clearly detailed in Ref. [4]. Moreover, it can be seen on the first microphones that the width of the autocorrelation peak varies with the size of the diaphragm. The larger the diameter of the diaphragm is, the wider the autocorrelation peak on the first microphones is. This is consistent with the fact that the large structure scale decrease with the jet diameter and that they radiate into the downstream direction. This phenomenon is not significant for the microphones in the sideline direction affected by the acoustic radiation of the small scale turbulence.

The correlation in the angular direction is then obtained by the cross-correlation between the different microphones of the directivity array. The cross-correlation function provides the correlation level between one signal and another delayed in time. It measures the causal linear link between these two signals and thus detect physical events that are common to these signals. In the present case, it provides the correlation level between the acoustic signals of the various microphones of the array and thus the correlation of the acoustic radiation into the angular direction. The cross-correlation is given by:

$$R_{mn}(\tau) = \frac{\langle p_m(t)p_n(t+\tau)\rangle}{\langle p_m^2(t)\rangle^{1/2}\langle p_n^2(t)\rangle^{1/2}}, \tag{8}$$

with m and n the microphone indices. Fig. 11 gives the maximum cross-correlation for the three tested diaphragms at NPR = 1.8. For example the first histogram R_{1n} shows the maximum of the cross correlation between the first microphone and its eight

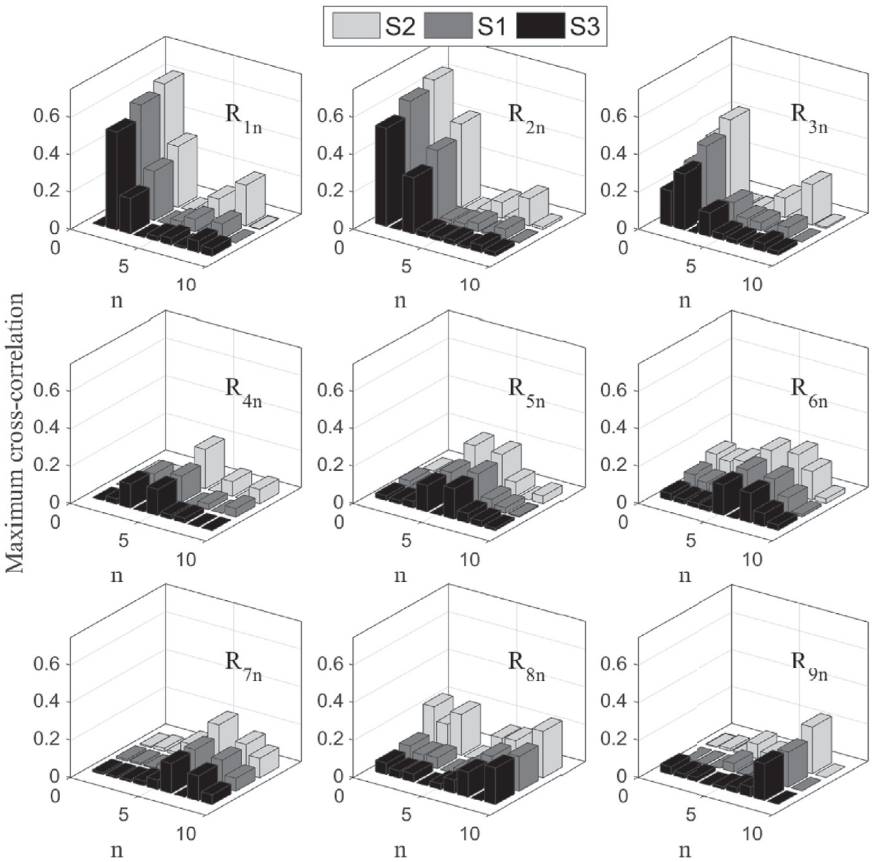

Fig. 11. Maximum cross-correlation at NPR = 1.8 for the three tested diaphragms.

neighbors. R_{11} corresponds to the maximum of autocorrelation (= 1) and is fixed to 0 on these histograms in order to maintain a visible range.

Again, as observed by Tam et al. [4], the behavior between the microphones in the downstream and sideline directions is very different. The maximum cross-correlation between the first three microphones (downstream direction) and their closest neighbors is much more important than on the following ones. Again, these results agree with the hypothesis of the double source. Indeed, the large coherent structures can also be expected to generate a more coherent acoustic radiation in the angular direction compared with the small scale turbulence which are more random. Two neighboring microphones will therefore be more likely to receive the same acoustic signal (resulting from the same disturbance) with a certain delay τ in the downstream direction which will result in an increase of the maximum cross-correlation. Moreover, the level of the maximum cross-correlation is observed to increase in the downstream direction when the diaphragm diameter decreases. No definite explanation has yet been found to explain this phenomenon.

Based on this dual source model and on the flow self-similarity assumption, Tam et al. [27] have attempted to derive generic spectra associated with each of these sources on axisymetric jets. They are named similarity spectra and will be designated by F and G in the following. F is associated with the radiation of the large coherent structures and corresponds to the far-field spectra of a perfectly expanded axisymmetric jet in the downstream direction (typically $\Theta = 30°$) while G is attributed to the radiation of the fine scale turbulence and corresponds to the spectra in the sideline direction (typically $\Theta = 90°$). These two spectra have been determined empirically using a large acoustic data base of jets. They show a very good agreement with a large number of experimental and numerical data [3,29]. Another similar work has been proposed by Kandula [30]. One of the main advantages of the latter model is that it takes into account a large number of parameters which influence the acoustic radiation such as the jet temperature, velocity, observation angle [31]… In the present case, only the shape of the spectra (named G2) will be considered. G2 is defined by:

$$G2 = \frac{(f/f_p)^{5/(4a)}}{\left[1 + (f/f_p)^2\right]^{9/(6a)}}, \tag{9}$$

where $a = \left[0.2 + \exp(-2M_c/\sin(\Theta/2))\right]^{0.35}$, M_c is the convective Mach number and f_p the frequency of the maximum mixing noise amplitude. Fig. 12 compares far field acoustic spectra at 30° and 90° for diaphragm S1 at NPR = 1.8 with the two previous

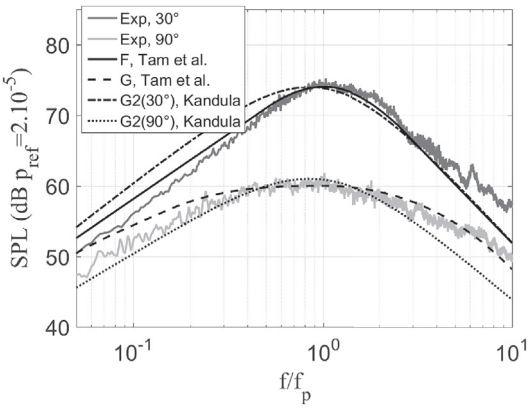

Fig. 12. Comparison of experimental far-field acoustic sepctra for S1 at NPR = 1.8 with similarity spectra of Tam et al. [27] and Kandula [30].

models.

A good agreement of the two models with the far-field acoustic radiated by diaphragms can be seen. At 30°, the G similarity spectra of Tam et al. gives a better prediction than Kandula's model. Only at high frequency, the level of the measurements is slightly above the prediction. At 90°, the predicted levels at low frequencies are slightly better with Kandula's model but are clearly underestimated at high frequencies. Tam et al. similarity spectra seem thus to offer the best prediction of the diaphragm mixing noise.

All these results show that the mixing noise generated by the valve equipped with an outlet diaphragm has similar characteristics as that of a jet issuing from a conventional nozzle. The set of results obtained on the latter configurations can therefore be applied to diaphragms.

4.2. Perforated disks

The same spectral analysis is now applied to the perforated plate cases. Normalized autocorrelation functions for perforated plates S1D1N1e1-3 and S1D3N3e1-3 are first shown in Fig. 13. The studied NPR is 1.8 so that the low NPR tonal noise is absent and does not disturb the analysis.

Very different results can be observed between the perforated plates shown in this figure. For those with the closest perforations first, similar results as for the diaphragm can be observed: the autocorrelation peak is much wider on the first two microphones than on the following ones. This indicates a much more coherent acoustic radiation in the propagation direction on these first microphones which again agrees with the mixing-noise modeling by the dual source. It indicates that for small spacing between the perforations, the small jets rapidly merge into a wider jet whose large scale structures dominate the downstream radiation. Similarly, as observed on the diaphragms, the reduction of the jet/perforation size (S1D1N1e1 to S1D3N3e1) causes a reduction of the autocorrelation peak width. This suggests a reduction of the large turbulent structure size responsible for this radiation. When the spacing of the perforations is now increased, a reduction of the autocorrelation peak width on the first microphones and an homogenization of the radiation on all the microphones can be observed. This is also associated with the appearance of negative parts on both sides of the main peak. This peak is more pronounced for the perforated plates with the smallest holes (S1D3N3e3) and demonstrates the presence of a coherent acoustic radiation. It thus appears that the increase of the perforation spacing causes a modification of the mixing-noise sources or the appearance of a new dominant source that seems to be coherent and radiating over a large angular range. This result is consistent with observations made on the directivity curves Fig. 7. To try to validate these observations, the maximum cross-correlation at NPR = 1.8 is plotted in Fig. 14 for the same perforated plates.

In the first bar chart corresponding to the disk with the largest perforations (S1D1N1e1-3), a significant effect of the perforation-spacing increase can be observed. When the perforations of the plate are the closest, similar results as those of the diaphragms are obtained: the maximum cross-correlation between a microphone and its closest neighbors is greater for the microphones in the downstream direction. This indicates a more coherent acoustic radiation in the angular direction of these microphones, which is in agreement with the model of the dual source of mixing noise. When the perforation spacing is now increased, the maximum cross-correlation increases on all the microphones. This indicates an increase of the acoustic radiation coherence in all angular directions. It is consistent with the observation made for the autocorrelations in Fig. 13: the increase of the perforation spacing seems to lead to the modification of the mixing-noise sources or to the emergence of a new coherent and omnidirectional one. On the second bar chart associated with the disks S1D3N3e1-3 composed of smaller perforations, the effect of the spacing increase is not clear. However, the coherence level on S1D3N3e1 is already seen to be clearly greater than for S1D1N1e1.

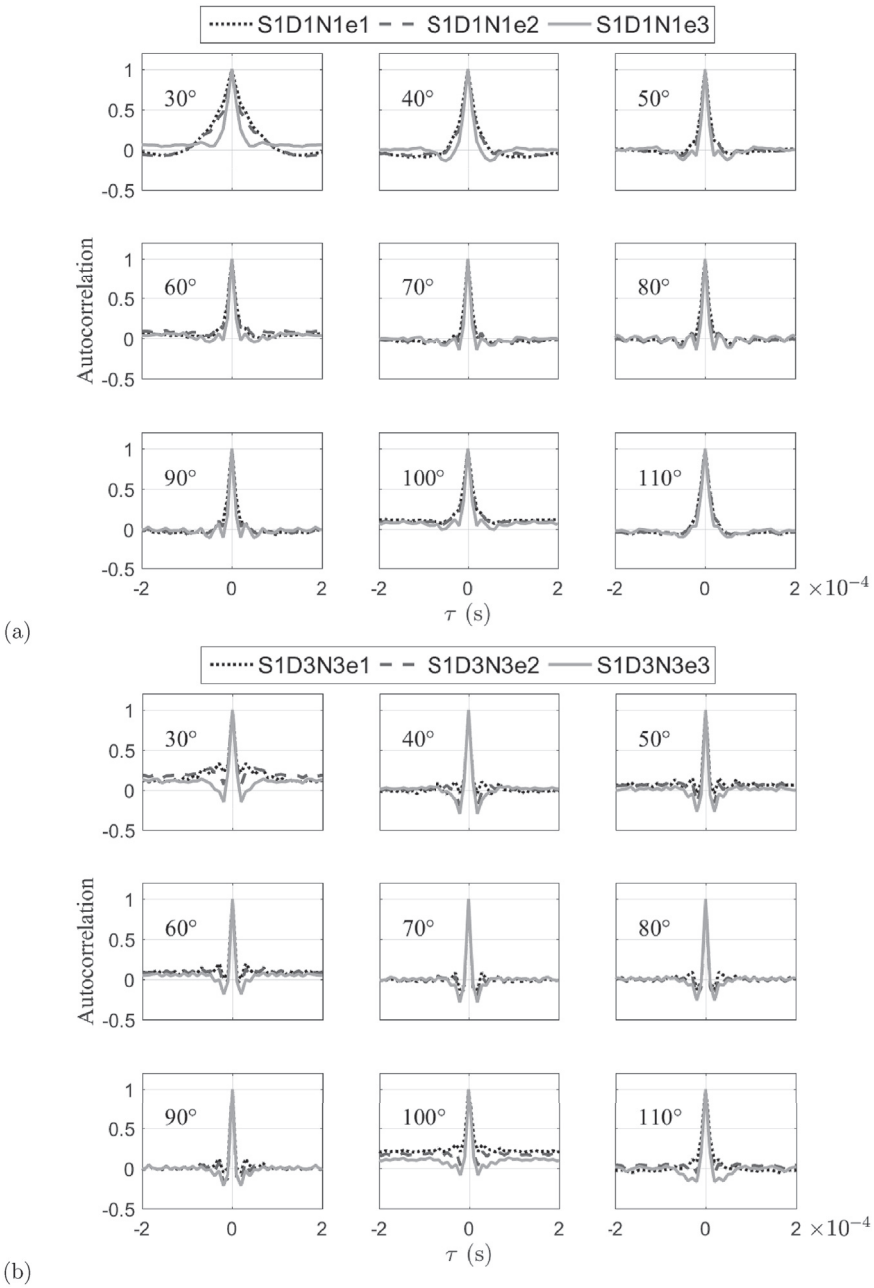

Fig. 13. Normalized autocorrelation at NPR = 1.8 for perforated plates with different perforation spacing: (a) S1D1N1e1-3 and (b) S1D3N3e1-3.

4.3. Proposed noise model

Having identified the geometrical parameters that allow modifying the broadband noise radiated by diaphragms and perforated plates, a simple sound prediction model can be developed to allow for the acoustic design of such systems. Three steps are necessary to carry out this modeling. The first one consists in determining the shape of the sound spectrum. During the second step, the spectrum is calibrated in frequency, whereas its amplitude is calibrated in the third step. For the first stage, Tam et al. and Kandula's similarity spectra are used [27,30]. Indeed, these spectra that were originally designed for jet noise have already been shown to very well predict the acoustic spectra radiated by diaphragms in Fig. 12. In this figure, the different spectra are normalized in frequency by the maximum amplitude frequency f_p. As discussed in the introduction, this frequency f_p can be determined for an unheated jet: the maximum amplitude at 90° (associated with small scale turbulence radiation) is obtained for $St \simeq 0.3$ and at 30° (associated with the radiation of large turbulent structures) for $St \simeq 0.2$ [3,6,7]. The amplitude of the

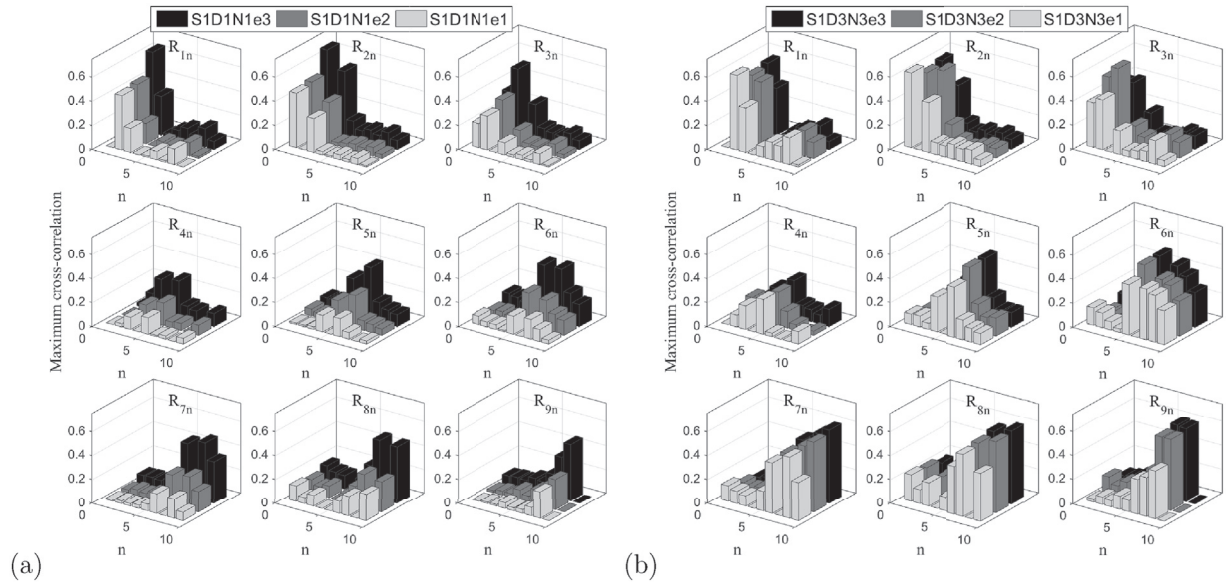

Fig. 14. Maximum cross-correlation at NPR = 1.8 for perforated plates with different perforation spacing: (a) S1D1N1e1-3 and (b) S1D3N3e1-3.

spectra can then be obtained by the eight power law derived from Lighthill's acoustic analogy [28]. Indeed, according to this law the total acoustic power W for subsonic jets reads:

$$W = K\rho_\infty c_\infty^{-5} D^2 U_j^8, \tag{10}$$

where ρ_∞ and c_∞ are the density and the sound speed in the ambient condition respectively and K a constant ($K \sim 3 \times 10^{-5}$). W is the total sound power radiated across any surface surrounding the jet. The mean square pressure $\langle p'^2 \rangle$ at a distance r in the far field of the jet mixing region obeys the scaling law [28,32,33]

$$\langle p'^2 \rangle \sim K\rho_j^2 c_\infty^{-4} (D/r)^2 U_j^8 / \left[\left(1 - M_c \cos(\Theta)\right)^2 + \alpha^2 M_c^2 \right]^{-5/2}, \tag{11}$$

where ρ_j is the exhaust gas density and α accounts for the finite decay time of the eddies. When comparing the SPL's obtained at a given observation angle, the Doppler amplification can be included into the calibration constant, if the convection velocity remains below $M_c \sim 1.5$ yielding:

$$\langle p'^2 \rangle \sim K'\rho_j^2 c_\infty^{-4} (D/r)^2 U_j^8. \tag{12}$$

In fact, studies of experimental spectra have shown an evolution closer to U_j^9 in the downstream direction and $U_j^{7.5}$ in the sideline direction [3,6,31]. This variation of the power law as a function of the observation angle has been attributed to the convection of the acoustic sources. In order to validate this evolution in the present measurements, the maximum amplitude of the mixing noise obtained with the diaphragms denoted by $\mathrm{SPL_{max}}$ is compared with the previous power law in Fig. 15 (a). The maximum amplitude is normalized by the diaphragm section S. Unlike the OASPL, the $\mathrm{SPL_{max}}$ is not affected by the strong tonal radiation that appears at high and low NPRs. The jet velocity U_j calculated here corresponds to the perfectly expanded jet velocity and is calculated with the isentropic relations.

For subsonic and low supersonic speeds, a very good agreement between the experimental data and the power law is obtained. Deviations appear only in the case of the diaphragm S2 for the lowest tested velocity. This gap can be explained by the presence of the low NPR tonal noise which is often associated with a middle frequency broadband hump (cf Sec. 6) and which modifies the broadband mixing-noise. The previous power law and the estimate of the jet velocity using isentropical relations being not adapted to the cases of supersonic choked jets, differences naturally appear between the experimental data and the power law. Moreover, for highly supersonic speeds, the Doppler effect modifies the power law to velocity to the power of 3. Hereafter, the prediction will therefore be limited to the subsonic and weakly supersonic regimes ($NPR \leq 2$).

Using these three steps, the diaphragm acoustic radiation at 90° and 30° can be predicted for unheated flow and for $NPR \leq 2$. Fig. 15 (b) compares the experimental results with the model prediction obtained for the diaphragm S1 at NPR = 1.6. The curves "Pred. Tam et al." and "Pred. Kandula" refer to the spectral shape from Refs. [27] and [30] respectively. As expected the best prediction is obtained at 30° with the similarity spectra of Tam et al. At 90°, however the latter being more flared, low frequencies are overestimated. At this angle, Kandula's model predicts the low frequency ranges better but the high frequencies

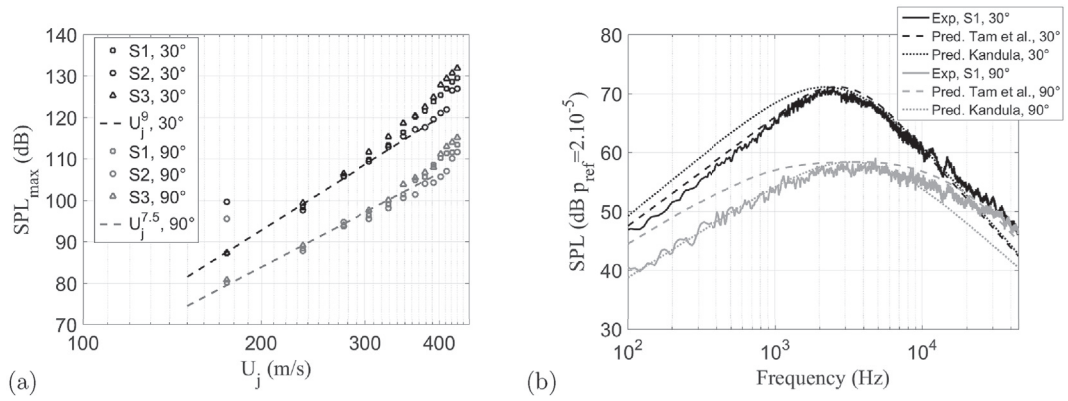

Fig. 15. (a) Comparison of Lighthill's power law with experimental data and (b) comparison of the experimental results with the prediction for the diaphragm S1 at NPR = 1.6.

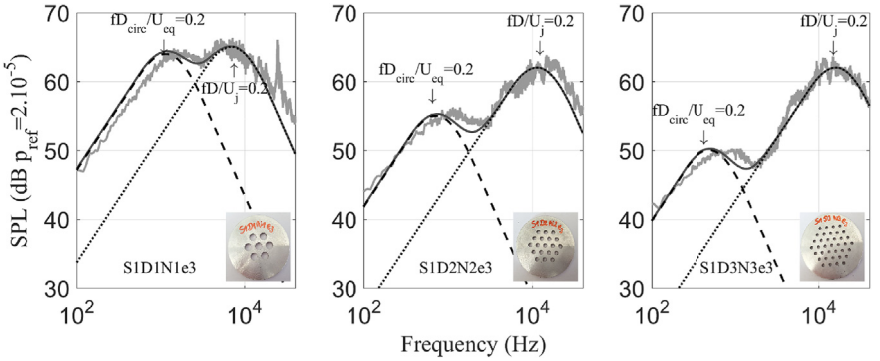

Fig. 16. Identification of the characteristic dimensions that govern the two humps for different grids at NPR = 1.6 and Θ = 30°.

are slightly underestimated. Nevertheless, the prediction using this very simple prediction model seems to give good results.

The same methodology is now applied to the perforated plate cases. As previously discussed, the mixing noise of the perforated plates is composed of two humps: PMH and MH. According to the literature and the present parametric study, the MH seems to be associated with the turbulence of the first two zones of the jet development called pre-merging and merging zones and PMH to the turbulence of the post-merging zone. To try to validate these assumptions, the characteristic dimensions that govern the two humps are analyzed on the different grids by considering 2 distinct contributions responsible for each of these humps. For this analysis, the similarity spectra of Tam et al. and the characteristic frequency of the mixing noise ($St \simeq 0.2$ at 30°) are used. By replacing the diameter D and the velocity U in the Strouhal expression with the appropriate characteristic dimensions, it appears that for the subsonic cases, the MH frequency seems to be related to a jet of diameter D (diameter of the perforations) and velocity U_j and PMH to an equivalent jet of diameter D_{circ} and velocity U_{eq} which conserves the momentum of all initial jets. By considering an isentropic flow and a constant temperature in the jet, the momentum conservation yields:

$$\rho_j\left(\frac{D_{circ}}{2}\right)^2 U_{eq}^2 = N\rho_j\left(\frac{D}{2}\right)^2 U_j^2. \tag{13}$$

The equivalent velocity is then expressed as:

$$U_{eq} = \sqrt{\frac{ND^2U_j^2}{D_{circ}^2}}. \tag{14}$$

The comparison of the spectra obtained by considering these two contributions with the experimental measurements is shown in Fig. 16. A good prediction of the frequency of the two humps is obtained. Only the frequency of the PMH is slightly underestimated. This can be explained by an underestimation of the flow velocity of the post merging zone. Moreover, these results seem to agree with the modeling of the multitube nozzle noise of Atvars [16]: the circumscribed circle is a good approximation of the size of the post merged jet which gathers all small isolated jets and which is responsible for the PMH while the perforation size gives the dimension of the initial jets responsible for the MH.

In summary, it is fairly simple to predict the shape and frequency of the two humps of the mixing noise for a given perforated plate. However it is still difficult to determine their levels accurately based only on the radiated acoustic field in particular for MH. Indeed, as mentioned in the introduction, the total sound power of MH is not the sum of all isolated jets but a fraction of them due to the shielding effect. A detailed study of the flow at the plate exit is now necessary to fully understand this shielding phenomena and to finalize this model.

5. Shock-associated noise study

When the regime becomes supersonic, an additional radiation due to the presence of shocks in the flow is observed. This radiation is characterized by multiple high frequency tones associated with a high frequency hump and is observed on all the diaphragms as well as on the grid with the closest perforations. The tonal component has been identified as screech and the broadband one as BBSAN.

Among the numerous studies on screech, several have proposed prediction models for the screech frequency f_s. One of the first models has been proposed by Powell [8] and considers that the temporal screech period t_s is equal to the sum of the time taken by the aerodynamic instabilities of the mixing layer to pass through the shock cells plus the time taken by the acoustic wave to return to the lips of the nozzle though the air along the flow. It is then given by:

$$f_s = \frac{U_c}{L_s(1+M_c)}, \tag{15}$$

where L_s is the shock cell size and U_c and M_c are the convection speed and the mach number respectively. Later, Tam et al. [15] re-formulated Powell's feedback loop theory by considering a close link between broadband shock associated noise and screech. According to their model, the screech is a special case of the BBSAN, and both mechanisms are generated by an interaction of instability waves with the quasi-periodic shock cells. Based on this mechanism, they proposed a new prediction model given by:

$$\frac{f_s D_j}{U_j} \simeq \frac{0.67}{(M_j^2-1)^{1/2}}\left[1+0.7M_j\left(1+\frac{\gamma-1}{2}M_j^2\right)^{-1/2}\left(\frac{T_a}{T_r}\right)^{-1/2}\right]^{-1}, \tag{16}$$

where T_a/T_r is the ratio of the ambient temperature to the reservoir temperature and γ is the adiabatic index. Hereafter we will compare this model tailored for unperfectly expanded supersonic jets issuing from conventional nozzle with the present measurements.

5.1. Diaphragms

In Fig. 17 (a), Tam et al.'s prediction model is compared with the frequencies obtained experimentally in the case of diaphragms. The ambient temperature is assumed to equal the reservoir temperature. In order to compare the frequencies obtained with the various diaphragms, the frequency analysis is done by studying the screech Strouhal number given by $St_s = f_s D_j/U_j$. D_j, U_j and M_j are calculated considering an equivalent perfectly expanded isentropic flow. A good prediction of the global evolution of the screech frequency for the various tested diaphragms with different diameters is obtained. The Strouhal number of the screech decreases when the Mach number increases. The ladder structures of the screech frequency highlighted by the gray dotted lines suggest the presence of different screech radiation modes that are not taken into account by the model. Indeed when the Mach number increases, the screech is characterized in particular by modifications of the frequency, acoustic directivity in the azimutal direction or convection velocity, which reflects the change of the radiation mode [8,35].

Another interesting feature of the screech is the directivity of the different screech frequencies. Indeed the main frequency and the different harmonics are characterized by a specific directivity. Based on Powell's screech model which considers a series of out-of-phase monopoles placed at the shock cell location, Norum [36] has obtained the noise directivity at these different frequencies, which indeed varies because of the different interferences between the sources. He has thus shown that for a C mode (characteristic of a supersonic jet at $3.3 < \mathrm{NPR} < 4.5$ according to [37]) the main screech frequency mainly radiates upstream and downstream, the first harmonic at 90° and 160° and the second harmonic at 60°, 100° and 160°. Similarly, based on their own screech model, Tam et al. [34] have shown that for the C mode, the main frequency mainly radiates at 161.9°, the first harmonic at 84.3° and 161.9° and the second harmonic at 63.3°, 104.5° and 161.9°. The latter preferred radiation directions are shown in Fig. 17(b) by the black arrows. By comparing these directivity models with the experimental results obtained for the diaphragm S1 at $\mathrm{NPR} = 3.6$ (Fig. 17 (b)), a good agreement can be observed. Note that the downstream direction for the main frequency predicted by Norum but not by Tam et al.'s model is identified in the present case. The other maximum radiation directions are very well predicted for each frequency, which indeed suggests the radiation of the C mode at this operating point in this configuration. Therefore, the characteristics of the screech appearing with the diaphragms are similar to that of supersonic jets issuing from conventional nozzles. The conclusions drawn for these jet flows can therefore be applied to the present configuration.

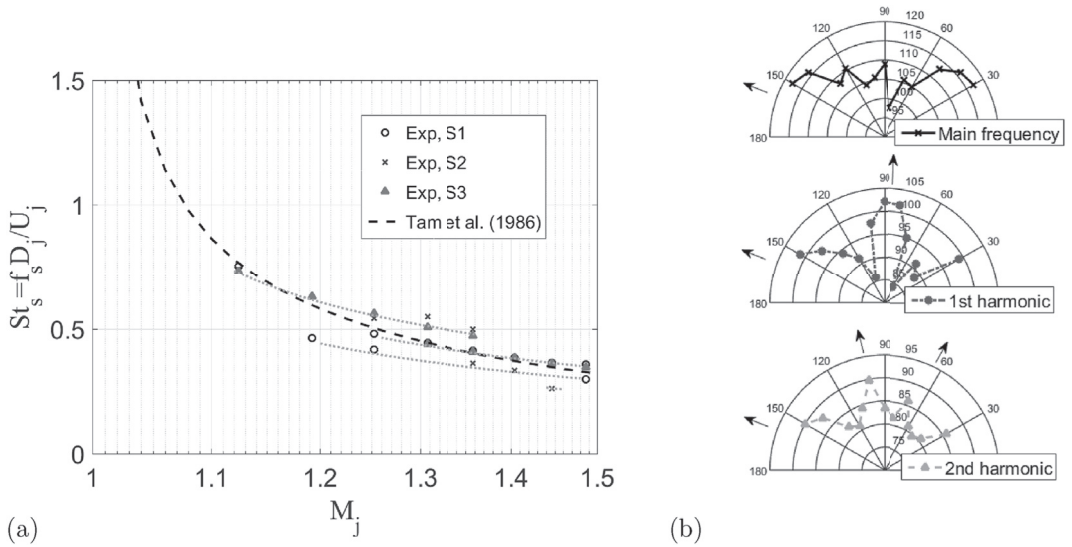

Fig. 17. (a) Evolution of the screech strouhal number as a function of the perfectly expanded Mach number and (b) comparison of the preferred radiation directions of the different screech harmonics given by Tam et al.'s model [34] (arrow) with the measurements in the case of the diaphragm S1 at NPR 3.6.

Table 2
Comparison between the screech frequency prediction and experimental data on the grid S4D4N4e4.

NPR	D	D_{eq}	D_{circ}	Experimental
3.2	96826 Hz	5169 Hz	3301 Hz	5392 Hz
3.4	91330 Hz	4875 Hz	3113 Hz	4808 Hz
3.6	86753 Hz	4631 Hz	2956 Hz	3816 Hz

5.2. Perforated disks

The focus is on the case of the grid S4D4N4e4 for which shock associated noise components are seen (Fig. 5 (d)). First, compared to a diaphragm, the shock noise appears at higher NPR (NPR $>$ 3.2 for S4N4D4e4 and NPR $>$ 2.4 for diaphragms, Fig. 8). It seems therefore that the presence of the perforations "delays" the generation of the shock noise. The previous prediction model of the screech frequency can be applied to this case by considering different characteristic dimensions: D the diameter of the perforations, D_{circ} the diameter of the circumscribed circle and D_{eq} the diameter of the equivalent diaphragm with similar cross-section. The prediction results obtained in each case are summarized in Table 2 and are compared with measurements.

The best prediction is obtained by taking as a characteristic dimension the diameter of the equivalent diaphragm. This tends to show that the shock cells are not formed on the isolated jets issuing from the perforations as observed for exemple by Zaman et al. [38] but on the grouped jets. The shock cells are thus larger, which explains the low frequency of the screech. A future study of the flow field is nevertheless necessary to confirm this hypothesis.

6. Low NPR tonal noise study

In addition to the sound sources discussed so far, the far-field acoustic spectra in Figs. 4 and 5 have shown high frequency tonal noise at the lowest NPR. This radiation can be seen on the smallest diaphragm (S2) and on most cases with perforated plates but at very different levels. Among the different cases, this tonal noise can be composed of a single tone (Fig. 18 (a)) or multiple high frequency tones named $f_1 \ldots f_n$ (Fig. 18 (b)) associated or not with a middle frequency hump. When several high frequency tones are present, medium frequency peaks named $f_{m_1} \ldots f_{m_n}$ may also appear.

In order to try to understand the origin of these different peaks in the cases of multiple high frequency tones, a Morlet wavelet study is carried out. This signal processing method allows to perform a time-frequency analysis of the acoustic signal with a better temporal resolution than a conventional Fourier transform with sliding window [39]. Fig. 18(c) gives the iso-contours of the square modulus of the wavelet transform coefficients normalized by its maximum for the first temporal segment of 8192 elements. A strong amplitude modulation can be observed at about 16190 Hz which corresponds to the dominant frequency of the tonal noise. This modulation has a period $\Delta T = 0.001$ s e.g. a modulation frequency $f_m = 1000$ Hz. This frequency corresponds to the first small peak at medium frequency and to the frequency spacing of the high frequency tones. The second medium frequency tone f_{m_2}, more intense, is a harmonic of this modulation frequency. In the same way, a bicoherence study is also carried out in this case to possibly explain the presence of the multiple high frequency tones $f_1 \ldots f_n$. Indeed this signal processing tool

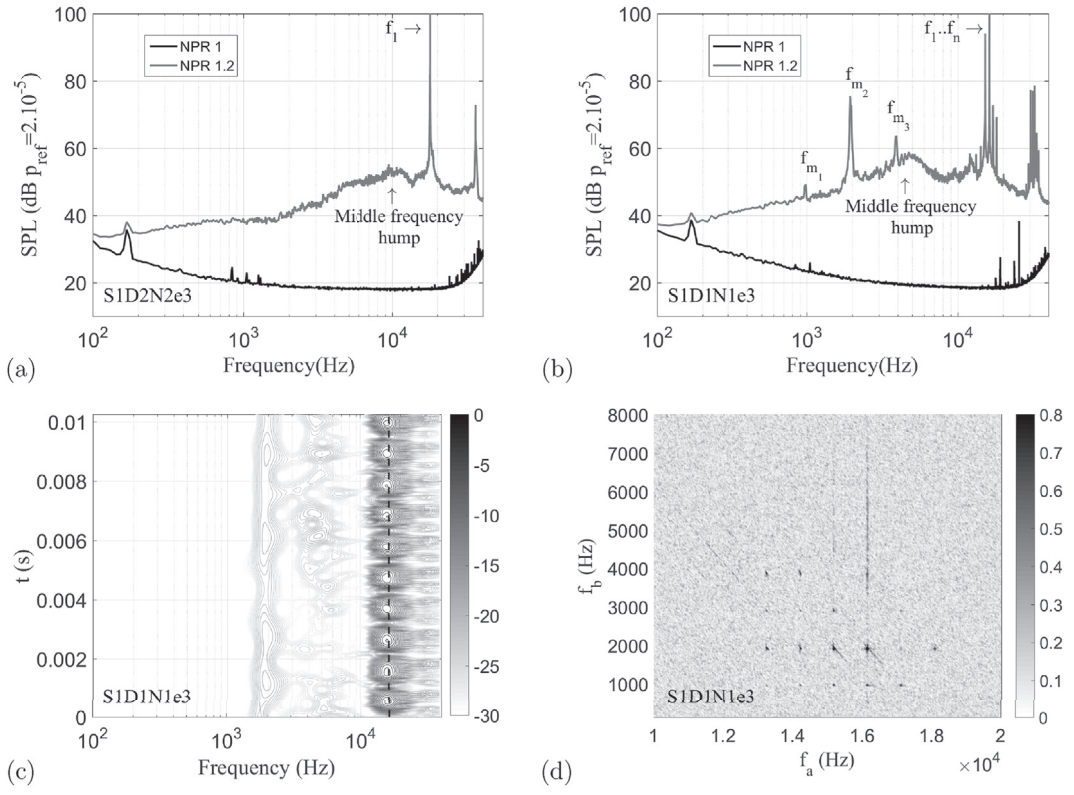

Fig. 18. NPR = 1.2 and $\Theta = 30°$: (a),(b) Far field acoustic spectra for S1D2N2e3 and S1D1N1e3 respectively; (c) normalized contour line mapping of the wavelet transform coefficients for the first temporal segment for S1D1N1e3 and (d) bicoherence of the acoustic signal for S1D1N1e3.

allows to highlight the phase couplings of three distinct frequencies f_a, f_b and f_c in a signal and can be interpreted as a trace of non-linear interactions. The bicoherence is bounded between 0 and 1: a high value of the bicoherence between two frequencies f_a and f_b means that the frequency $f_c = f_a + f_b$ is generated by a non-linear interaction between f_a and f_b. In other words, the frequency f_c is not generated by a new source but by a non-linear interaction of the sources a and b at the frequencies f_a and f_b respectively. The bicoherence in the case of the perforated plate S1D1N1e3 at NPR 1.2 is plotted in Fig. 18 (d) and the frequencies with a strong bicoherence as well as the frequencies of the high frequency tones are summarized in Table 3. It can be observed that the different frequencies of the high frequency tones can be obtained by a combination of two frequencies between which a strong bicoherence appears. High frequency tones then seem to be generated by a non-linear interaction between a modulation frequency and a high frequency peak. In summary, the mean frequency lines correspond to the modulation frequency (and its harmonics) of the dominant high-frequency tones while the other secondary high frequency peaks are obtained by non-linear interactions between these different frequencies. Possibly a single noise source is therefore responsible for the different tonal noise scenario.

A first possible explanation for this tonal noise component is the appearance of vortex shedding because of the von Karman street developing between the different perforations as observed experimentally by Zaman et al. [38] in their investigation of the acoustic effects of the splitting of a single rectangular jet into several smaller jets. Their measurements were performed for subsonic and supersonic speeds and they noted the emergence of a high frequency tonal noise at low speeds for cases where the jet is divided. This tonal radiation was attributed to vortex-shedding noise caused by the separations of different jets and is characterized by a Strouhal number $St = 0.2$ based on this separation thickness. This therefore induces a linear evolution of the frequency as a function of the flow velocity for a given separation thickness. In the present case however, this tonal noise does not seem to be influenced by the perforations spacing as shown in Fig. 19 which present the evolution of the tonal noise frequency as a function of the velocity calculated by considering an isentropic flow. Indeed the tonal noise frequency seems to evolve according to the square root of the flow velocity and does not seem to be affected by the perforation diameter, the perforation spacing, the perforation number or cross-section. Moreover, this tonal noise seems to have different modes depending on the flow velocity and the geometrical parameters emphasized by the dotted lines. Finally, it can be noted that this radiation also appears in the case of the diaphragm S2 for which the von Karman vortex shedding cannot be created. Therefore, this explanation does not seem to hold in the present case.

Another possible physical explanation of this tonal noise may be the appearance of vortex shedding due to the sharp flow restriction and the inlet sharp-edges of the diaphragms and perforated plates. When these instabilities are associated with

Table 3
Comparison of frequencies formed by non-linear interactions f_c with frequencies of the high frequency tones f_n.

f_a (Hz)	f_b (Hz)	$f_c = f_a + f_b$ (Hz)	f_n (Hz)
13260	975	14235	$f_1 = 14230$
13260	1950	15210	$f_2 = 15210$
13260	2901	16161	$f_3 = 16190$
13260	3877	17137	$f_4 = 17140$
14230	975	15205	$f_5 = 18170$
14230	1950	16180	
14230	2926	17156	
14230	3902	18132	
15180	975	16155	
15180	1976	17156	
15180	2928	18108	
16160	975	17135	
16160	1951	18111	
17110	975	18085	

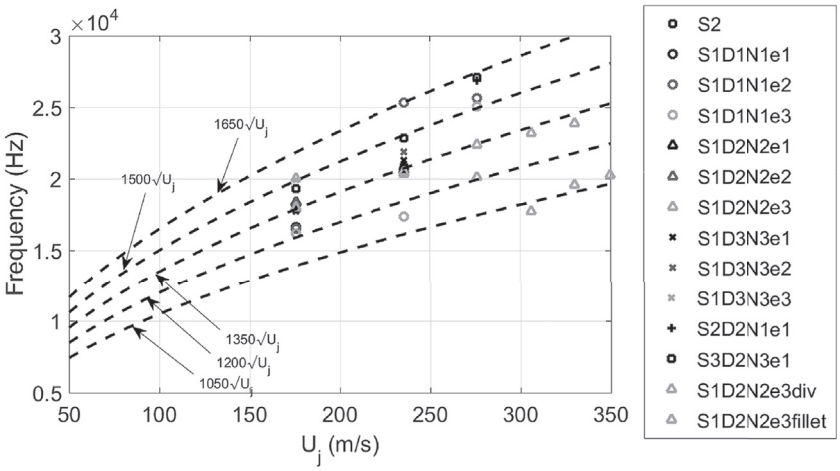

Fig. 19. Evolution of the frequency of the low NPR tonal noise as a function of the velocity.

a hydrodynamic or an acoustic feedback, a whistling phenomenon can occur. A feedback can for example appear when the vortices generated at the perforation inlet reach a region where the steady velocity exhibits a gradient. The abrupt expansion at the exit of the perforations may be responsible for such velocity gradient. The resulting vortex deformation would generate sound waves, some of which propagating back to the perforation inlet and triggering the vortex formation. This inlet/outlet feedback could then explain the high amplitude tones found in the low NPR spectra. Similar phenomenon has been extensively studied mainly for low Reynolds and Mach numbers [40–45]. In Ref. [45], in particular, it is outlined that replacing the sharp edge at the exit of a whistling nozzle by a horn can induce an increase of the whistling potential of this nozzle. A similar behavior is observed for the plates S1D2N2e3div/fillet for which the outlet geometry of the perforation has been modified by adding a fillet or a divergent aperture. The tonal noise then persists for a larger NPR range. This mechanism therefore seems to be a good candidate for the low NPR tones of the present study. It requires however additional flow measurements to be validated.

7. Conclusion

An extensive experimental study of the noise radiated by the discharge of a high pressure flow through diaphragms and perforated disks has been carried out. In practical applications such devices are often placed inside ducts with possibly variable cross-sections. In the present study these diaphragms and perforated disks are however placed at the exit of a constant area duct so that there is no modification of the flow or the sound propagation by the downstream part of the duct. Subsequently, the flow leaving the perforated plates or diaphragms consists of multiple or single jets in free-field. The study has been conducted for a large range of subsonic and supersonic regimes as well as for a number of geometrical configurations, and has shown several acoustic behaviors.

In all cases, the far field acoustic radiation is dominated by a broadband noise associated with the mixing in the jet shear layers. In the case of diaphragms, similar characteristics as the mixing noise of a jet issuing from a conventional nozzle has been observed. The two contributions of this source associated with the radiation of the large coherent turbulent structures as well

as the small scale turbulence have indeed been observed. In the case of the perforated plates, the multiple micro-jets generated merge into a larger jet; the broadband noise is modified accordingly and exhibits two distinct humps. The high frequency one is associated with the turbulence of the pre-merging and merging regions of the multiple micro-jets and is related to the size of the perforations while the low frequency hump is associated with the turbulence of the post merging zone and scales with the size of the circumscribed circle. The parametric study has also shown that the modification of the geometrical parameters of the perforated plates changes the level and the frequency of these two humps. For example increasing the perforation spacing for a constant cross section, perforation number and perforation size leads to a later merging of the jets issuing from the perforations and decreases the low frequency hump while increasing the high frequency hump. This makes it possible in particular to reduce the acoustic level in the audible range by shifting the acoustic energy into the ultra sound range.

When the operating regime becomes supersonic, shock associated noise (broadband shock associated noise and screech) has been observed for the diaphragm cases and for the perforated plate with the closest perforations. Again the characteristics of this radiation (frequency and directivity) for the diaphragm cases are similar to those observed on shocked jets from convectional nozzles that are not fully expanded. In particular, Tam et al.'s [34] model allows to accurately predict the screech frequency. In the perforated plate cases, this radiation seems to only appear if the perforations are very close to each other ($e/D \simeq 0.2$ in S1D4N4e4). In this case the perforated disk seems to behave acoustically like a diaphragm.

Finally, a new acoustic behavior has been observed at the lowest NPR. It appears for the smallest diaphragm and for most perforated plates but with very different levels. It is also emphasized by the modification of the perforations (divergent shape or fillets). This radiation is characterized by one or several high frequency tones associated with a middle frequency hump. In multi-tone cases, the different peaks have been studied by high order spectral analysis and are explained by the presence of an amplitude modulation of the main tone. This radiation is possibly associated with the generation of vortex shedding due to the sharp section reduction and sharp edge combined with a resonance at the perforation outlet.

A detailed study of the flow and the near acoustic field is now necessary to confirm the analysis of the low NPR tonal noise and to provide the level of MH in the perforated plate cases.

Acknowledgements

This work was performed within the framework of the Labex CeLyA of the Université de Lyon, within the programme "Investissements d'Avenir" (ANR-10- LABX-0060/ANR-11-IDEX-0007) operated by the French National Research Agency (ANR) and is also supported by the industrial Chair ADOPSYS co-financed by Safran Aircraft Engines and the ANR (ANR-13-CHIN-0001-01).

Appendix A. Supplementary data

Supplementary data related to this article can be found at https://doi.org/10.1016/j.jsv.2018.07.036.

References

[1] K. Zaman, Effect of initial condition on subsonic jet noise, AIAA J. 23 (9) (1984) 1370–1373.
[2] C. Bogey, C. Bailly, An analysis of the correlations between the turbulent flow and the sound pressure fields of subsonic jets, J. Fluid Mech. 583 (2007) 71–97.
[3] C. Bailly, C. Bogey, O. Marsden, T. Castelain, Subsonic and Supersonic Jet Mixing Noise, VKI Lecture Series 2016-04, 2016, pp. 1–62.
[4] C. Tam, K. Viswanathan, K. Ahuja, J. Panda, The sources of jet noise: experimental evidence, J. Fluid Mech. 615 (2008) 253–292.
[5] J. Panda, R. Seasholtz, Experimental investigation of density fluctuations in high-speed jets and correlation with generated noise, J. Fluid Mech. 550 (2002) 91–130.
[6] C. Bogey, S. Barré, V. Fleury, C. Bailly, D. Juvé, Experimental study of the spectral properties of near-field and far-field jet noise, Int. J. Aeroacoustics 6 (2) (2007) 73–92.
[7] C. Bogey, C. Bailly, Investigation of downstream and sideline subsonic jet noise using large eddy simulation, Theor. Comput. Fluid Dynam. 20 (1) (2006) 23–40.
[8] A. Powell, On the mechanism of choked jet noise, Proc. Phys. Soc.Sect. B 67 (4) (1954) 313–327.
[9] J. Panda, An experimental investigation of screech noise generation, J. Fluid Mech. 378 (1999) 71–96.
[10] G. Raman, Supersonic jet screech: half-century from powell to the present, J. Sound Vib. 225 (3) (1999) 543–571.
[11] B. André, étude expérimentale de l'effet de vol sur le bruit de choc de jets supersoniques sous-détendus (experimental study of fhe flight effects on the shock-associated noise of underexpanded supersonic jets), École Centrale de Lyon, 2012 (Ph.D. thesis).
[12] C. Tam, Supersonic jet noise, Annu. Rev. Fluid Mech. 27 (1995) 17–43.
[13] M. Harper-Bourne, M. Fisher, The Noise from Shock Waves in Supersonic Jets, AGARD CP 131 19, 1973, pp. 1–14.
[14] C. Tam, H. Tanna, Shock associated noise of supersonic jets from convergent-divergent nozzles, J. Sound Vib. 81 (3) (1982) 337–358.
[15] C. Tam, J. Seiner, J. Yu, Proposed relationship between broadband shock associated noise and screech tones, J. Sound Vib. 110 (2) (1986) 309–321.
[16] J. Atvars, C. Wright, C. Simcox, Supersonic jet noise suppression with multitube nozzle/ejectors, in: 2nd AIAA Aeroacoustics Conference, Hampton, VA, USA, 1975.
[17] S. Sheen, Effect of exit spacing in a multiple-jet nozzle on noise levels at audible frequencies, J. Occup. Environ. Hyg. 8 (2011) 349–356.
[18] J. Atvars, G. Paynter, D. Walker, C. Wintermeyer, Development of Acoustically Lined Ejector Technology for Multitube Jet Noise Suppressor Nozzles by Model and Engine Tests over a Wide Range of Jet Pressure Ratios and Temperatures, NASA Contractor Report NASA CR-2382, 1974, pp. 1–338.
[19] D. Regan, W. Meecham, Multitube turbojet noise-suppression studies using crosscorrelation techniques, J. Acoust. Soc. Am. 63 (6) (1978) 1753–1767.
[20] W. Meecham, D. Regan, Cross-correlation of noise produced inside a hot turbojet exhaust with and without suppression, in: 2nd AIAA Aeroacoustics Conference, Hampton, VA, USA, 1975.
[21] V. Gray, O. Gutierrez, D. Walker, Assessment of Jets as Acoustic Shields by Comparaison of Single and Multitube Suppressor Nozzle Data, NASA Technical Memorandum NASA TM X-71450, 1973, pp. 1–21.
[22] D. Middleton, P. Clark, Assessment and Developpement of Methods of Acoustic Performance Prediction for Jet Noise Suppressors, UTLAS Technical Note 134, 1969, pp. 1–49.

[23] K. Eldred, R. White, M. Mann, M. Cottis, Suppression of jet noise with emphasis on the near field, Tech. Doc. Rep. 62 (376) (1963) 1–235.
[24] T. Balsa, The shielding of a convected source by an annular jet with an application to the performance of multitube suppressors, J. Sound Vib. 44 (2) (1976) 179–189.
[25] S. Sheen, Y. Hsiao, On using multiple-jet nozzles to suppress industrial jet noise, J. Occup. Environ. Hyg. 4 (2007) 669–677.
[26] K. Viswanathan, Instrumentation considerations for accurate jet noise measurements, AIAA J. 44 (6) (2006) 1137–1149.
[27] C. Tam, M. Golebiowski, J. Seiner, On the two components of turbulent mixing noise from supersonic jets, in: 2nd AIAA/CEAS Aeroacoustics Conference, State Collage, PA, USA, 1996.
[28] M. Lighthill, On sound generated aerodynamically. I. General theory, Proc. Roy. Soc. Lond. 211 (1107) (1952) 564–587.
[29] K. Viswanathan, Analysis of the two similarity components of tubulent mixing noise, AIAA J. 40 (9) (2006) 1735–1744.
[30] M. Kandula, On the scaling laws and similarity spectra for jet noise in subsonic and supersonic flow, Int. J. Acoust. Vib. 13 (1) (2008) 3–16.
[31] H. Tanna, An experimental study of jet mixing noise part 1: turbulence mixing noise, J. Sound Vib. 50 (3) (1977) 405–428.
[32] J.F. Williams, The noise from turbulence convected at high speed, Phil. Trans. Roy. Soc. A. 255 (1963) 469–503.
[33] H. Ribner, W. Meecham, The generation of sound by turbulent jets, Adv. Appl. Mech. 8 (1964) 103–182.
[34] C. Tam, S. Parrish, K. Viswanathan, The harmonics of jet screech tones, in: 19th AIAA/CEAS Aeroacoustics Conference, Berlin, Germany, 2013.
[35] J. Panda, G. Raman, K. Zaman, Underexpanded screeching jets from circular, rectangular and elliptic nozzles, in: 3rd AIAA/CEAS Aeroacoustics Conference, Atlanta, GA, USA, 1997.
[36] T. Norum, Screech suppression in supersonic jets, AIAA J. 21 (2) (1983) 235–240.
[37] A. Powell, Y. Umeda, R. Ishii, Observations of the oscillation modes of chocked circular jets, J. Acoust. Soc. Am. 95 (5) (1992) 2823–2836.
[38] K. Zaman, J. Bridges, A. Fagan, C. Brownn, An experimental investigation of jet noise from septa nozzles, in: 22nd AIAA/CEAS Aeroacoustics Conference, Lyon, France, 2016.
[39] C. Torrence, G.P. Compo, A practical guide to wavelet analysis, Bull. Am. Meteorol. Soc. 79 (1) (1998) 61–78.
[40] A. Anderson, Metastable jet-tone states from sharp-edged, circular, pipe-like orifices, J. Acoust. Soc. Am. 27 (1) (1954) 13–21.
[41] A. Anderson, Structure and velocity of the periodic vortex-ring flow pattern of a primary pfeifenton (pipe tone) jet, J. Acoust. Soc. Am. 27 (6) (1955) 1048–1053.
[42] P. Testud, Y. Aurégan, P. Moussou, A. Hirschberg, The whistling potentiality of an orifice in a confined flow using an energetic criterion, J. Sound Vib. 325 (2009) 769–780.
[43] R. Lacombe, Sifflement de diaphragmes en conduit soumis à un écoulement subsonique turbulent (whistling generated by ducted diaphragm at subsonic regimes), Université du Maine, 2011 (Ph.D. thesis).
[44] B. Karthik, S. Chakravarthy, R. Sujith, Mechanism of pipe-tone excitation by flow through an orifice in a duct, Int. J. Aeroacoust. 7 (3–4) (2008) 321–348.
[45] A. Hirschberg, J. Bruggeman, A. Wijnands, N. Smits, The “Whistler Nozzle” and horn as aero-acoustic sound sources in pipe systems, Acoustica 68 (1989) 157–160.